Investigations of nanocarbons and related materials

A Thesis

Submitted for the degree of

Master of Science [Engg.]

By

Pramoda K.

New Chemistry Unit

Jawaharlal Nehru Centre for Advanced Scientific Research

(A Deemed University)

Bangalore-560 004

July-2013

Dedicated to my teachers, family and friends

Declaration

I hereby declare that the matter embodied in this thesis entitled **"Investigations of nanocarbons and related materials"** is the result of investigations carried out by me under the supervision of Prof. C. N. R. Rao, FRS at the New Chemistry Unit, Jawaharlal Nehru Centre for Advanced Scientific Research, Bangalore, India and that it has not been submitted elsewhere for the award of any degree or diploma.

In keeping with the general practice in reporting scientific observations, due acknowledgement has been made whenever the work described is based on the findings of other investigators.

_____

Pramoda K.

CERTIFICATE

I hereby certify that the matter embodied in this thesis entitled **"Investigations of nanocarbons and related materials"** has been carried out by Mr. Pramoda K. at the New Chemistry Unit, Jawaharlal Nehru Centre for Advanced Scientific Research, Bangalore, India under my supervision and that it has not been submitted elsewhere for the award of any degree or diploma.

Prof. C. N. R. Rao, FRS

(Research Supervisor)

Acknowlegments

I am extremely thankful to my research supervisor Prof. C. N. R. Rao, FRS and I take this opportunity to express my immense gratitude to him. He not only introduced me to the fascinating field of Material Science but also has helped me with his invaluable guidance and constant encouragement. He has taught me the various facts of science, the way of understanding the problem and how to maintain level headed approach when problems do not work.

My deepest thanks to Mrs. Indumati Rao and Mr. Sanjay for their affection and hospitality.

I would like to express my sincere thanks to Dr. A. Govindaraj who has helped me a great deal in carrying out the various experiments. It has been a good learning experience working with him in the lab.

I am grateful to the administration of JNCASR, especially chairman of NCU Prof. C. N. R. Rao and CPMU chairman Prof. S. Balasubramanian, for allowing me to use all the facilities in JNCASR required for my experimental work.

I am thankful to Usha madam, Anil, Vasu, Selvi, Dr.Karthik (TEM), Dr.Basavaraj (VEECO), Kishore (XPS), Dr. Joy and Mahesh for their help with the various characterization techniques. I thank Srinath for his technical help.

PREFACE

The thesis consists of four chapters of which the first chapter is a brief overview of graphene. Chapter 2 deals with synthesis of chemically bonded metal oxides to the functionalized graphene surface. Synthesis of composites of inorganic analogues of graphene is presented in Chapter 3. This chapter consists, synthesis of composites by both physical and chemical methods.

Chapter 4 deals with synthesis, functionalization and doping of single-walled carbon nanohorns. Part 1 deals with the synthesis, different ways of functionalization and solubilization. Amidation solubilize SWNHs in organic solvents whereas wrapping with surfactant gives water soluble SWNHs. Non-covalent π-π interaction with a coronene derivative solubilize SWNHs in polar solvents. Band gap engineering of graphene structural analogues can be effectively achieved by doping suitably. Part 2 deals with the routes of doping SWNHs with boron and nitrogen. The submerged arc discharge technique to prepare SWNHs has been effectively employed to chemically dope SWNHs.

CONTENTS

CHAPTER 3: COMPOSITES OF INORGANIC GRAPHENE ANALOGUES

3.1 Synthesis, characterization and electrical properties of nanocomposite of Molybdenum disulphide with PANI

3.2 Electrical properties of nanocomposite of molybdenum disulphide with graphene

3.3 Graphene-Few-layer boron nitride composites

CHAPTER 1
GRAPHENE: AN OVERVIEW

1.1 Nature of graphene and related aspects

1.1.1 Allotropes of carbon

Carbon is one of the most interesting elements in the periodic table and it plays a unique role in nature. Carbon has the ability to form very long chains of interconnecting C-C bonds which is known as catenation. Due to catenation, carbon forms the highest number of compounds compared to any other element. The capability of carbon atoms to form complicated networks [1] is fundamental to organic chemistry and forms the basis for the existence of life. Elemental carbon forms many allotropes [Figure 1] such as diamond, graphite, fullerenes [2-4] and nanotubes [5].
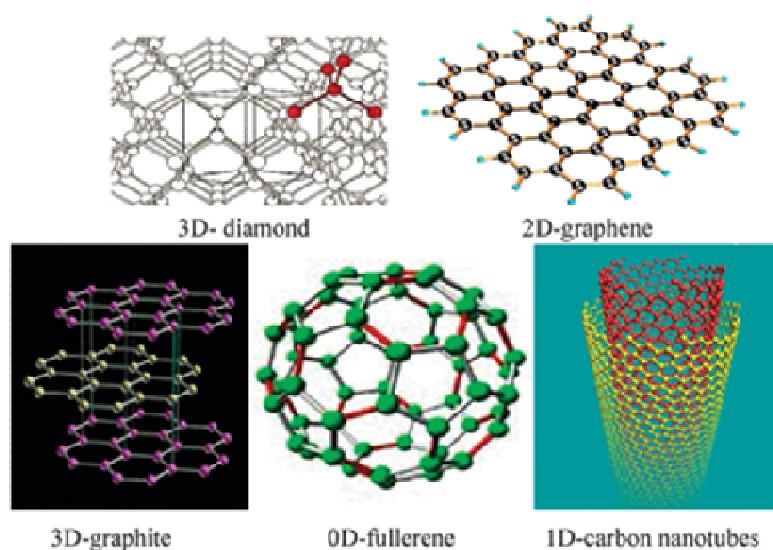
Figure 1. *3D, 2D, 1D and 0D forms of graphene.*

1.1.2 Brief history of graphene

The two-dimensional form of carbon called graphene (or '2D graphite') is the mother of all graphitic forms. It is a single-layer of carbon atoms tightly packed into a honeycomb lattice which can be either wrapped up into 0D fullerenes, rolled into 1D nanotube or stacked into 3D graphite (Figure 2). Although recently, there has been a great surge in graphene research. Graphene-related materials produced from graphite oxide (GO) were already reported in 1962 and the chemical modifications of graphite were performed as early as 1840. In the 1940s [6] a number of theoretical studies suggested that the graphitic layers in their isolated form might exhibit extraordinary characteristics.
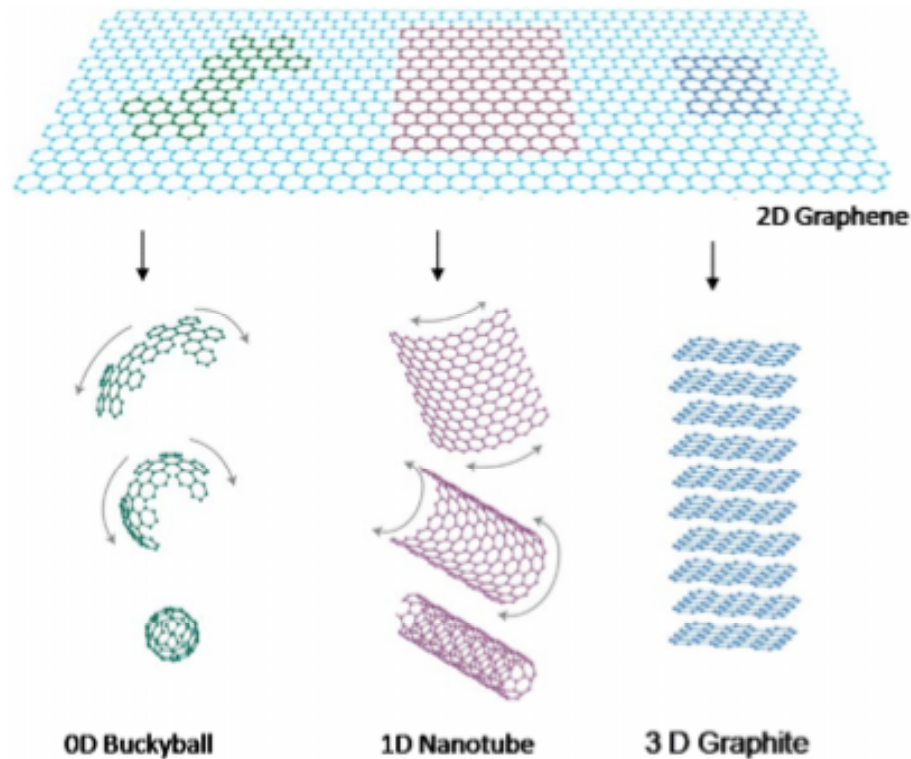
Figure 2. *Mother of all graphitic forms. (From ref. [14]).*

Following the theoretical studies, later, several researchers made attempts to prepare graphene by employing different procedures like thermal deflagration of GO, mechanical exfoliation of GO followed by reduction [7], sublimation of silicon from single crystals of silicon carbide (0001) [8] and by micromechanical approach [9,10]. Most of these procedures resulted in multi-layered graphene and the products were not characterized properly. In 2004 Geim and co-workers employed the same "micro-mechanical approach" reported by Roscoe *et al.* [10] and found that the approach enabled the generation of extremely thin graphene films with a single or few layers [11-13]. The graphene samples have been characterized by a variety of microscopic and other physical techniques like atomic force microscopy (AFM), transmission electron microscopy (TEM), scanning tunnelling microscopy (STM) and Raman spectroscopy [14]. It has been shown that graphene is a two-dimensional semi-metal with a tiny overlap between valence and conductance bands. Graphene exhibits a strong ambipolar electric field effect with very high concentrations of electrons and holes, up to 10^{13}/cm^2 and room-temperature mobilities of ~10,000 cm^2/V.s [11]. It is interesting that single-layer graphene placed on a silicon wafer with a 300 nm thick layer of SiO_2, becomes visible in an optical microscope [15].

1.1.3 Types of graphene

Graphene can be classified into three types: single-, double- and few- (3 to <10) layer graphenes. Films containing more than 10 layers can be considered as thin films of graphite. It was shown that the electronic structure of graphene rapidly evolved with the number of

layers, approaching the 3D limit of graphite at 10 layers [16]. Moreover, only single- and bi-layer graphenes have simple electronic spectra: they are both zero-gap semiconductors (they can also be referred to as zero-overlap semimetals) with a single type of electrons and holes.

After more than two layers, the spectra become increasingly complicated by the overlapping of the conduction and valence bands [16] and thus by the appearance of several types of charge carriers.
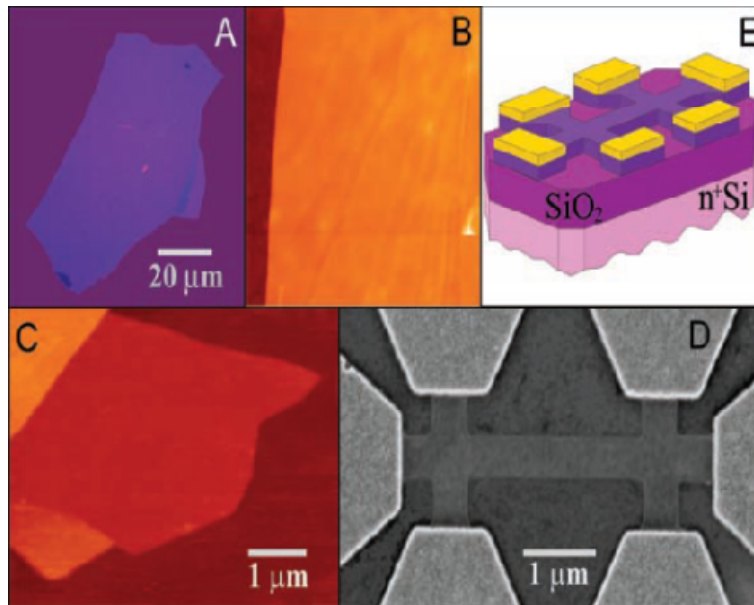
Figure 3. *Graphene films.(A) Photograph (in normal white light) of a relatively large multilayer graphene flake with thickness ~3 nm on top of an oxidized Si wafer. (B) Atomic force microscope (AFM) image of 2 μm by 2 μm area of this flake near its edge. Colors: dark brown, SiO₂ surface; orange, 3 nm height above the SiO₂ surface. (C) AFM image of single-layer graphene. Colors: dark brown, SiO₂ surface; brown-red (central area), 0.8 nm height; yellow-brown (bottom left), 1.2 nm; orange (top left), 2.5 nm. Notice the folded part of the film near the bottom, which exhibits a differential height of ~0.4 nm. (D) Scanning electron microscope image of an experimental device prepared from FLG. (E) Schematic view of the device in (D). (From ref. [11]).*

1.1.4 Synthesis of Graphene

At the beginning, the graphene fabrication was limited to micromechanical cleavage from graphite, it was also the method by which graphene was first isolated for property study. This way is often referred to as a scotch-tape technique, which relies on destroying Van der Waals force between graphite layers. Geim's group first isolated graphene from platelets of highly oriented pyrrolytic graphite (HOPG) [11]. The next method for graphene fabrication is chemical cleavage from graphite, which is an improvement of micromechanical cleavage. Graphene made from chemical cleavage can reap larger quantities. The single sheet is fabricated from graphite oxide. Due to the existence of oxygen based functional groups, the atomic planes of graphite are partially detached by intercalation. After ultrasonication for several hours, these samples are exfoliated to create stable aqueous dispersions of individual sheets. After deposition, graphene oxide can be reduced to graphene chemically or by thermal annealing [17]. Although the thickness is not consistent, which varies between one and four layers of carbon, the optical properties still match to those of graphene fabricated by micromechanical cleavage method. The small lateral dimension in tens of microns, however, hinders the application of graphene by this method.

The graphene, grown epitaxially on SiC substrates and patterned via standard lithographic procedures, has been proposed as a platform for carbon-based nanoelectronics and molecular electronics in recent studies [18, 19]. The epitaxial graphene was produced on the Si terminated (0001) facet of single-crystal 6H-SiC by thermal desorption of Si [20]. After the surface is oxidized or reduced in H_2, samples are heated by electron bombardment in ultra high vacuum (1.33×10^{-8} Pa) to 1000 °C to remove the oxide. Then, samples are

heated again to temperatures in the range of 1250 °C to 1450 °C for 1–20 min. After these processes, thin graphene layers are formed and the layer thickness is determined predominantly by the temperature [18]. The shortcoming of the epitaxial graphene on SiC is presence of large number of defects in the layer besides it hard to transfer to other substrates.

Chemical vapour deposition (CVD) has the potential for large-area production. Graphene, made by CVD on silicon wafer with nickel layer as catalyst, has achieved the lateral dimensions centimetre in size. Groups at MIT and in Korea [21, 22] have developed a simple method to grow and transfer the high-quality stretchable graphene films using CVD technology on nickel layer. The mechanism is based on precipitation of carbon, where Ni and C atoms form a solid solution in CVD after heating. Since the solubility of C in Ni is temperature-dependent, C atoms precipitate and form graphene layer on the Ni surface upon sharply cooling the sample [22] and the number of layers of graphene depends on the concentration of C precipitated on Ni. However, Li *et al*. [23] recently fabricated graphene films on copper foils. They concluded that the thickness of graphene films were independent on exposure time and the low solubility of carbon in copper made this growth process self-limiting. The precipitation mechanism did not work on copper substrate. Therefore, the mechanism of CVD growth of graphene needs additional experiments to be carried out to fully understand the process. Arc-discharge is the most efficient method of making few-layer graphene and has been developed by Rao *et al.* [24]. DC-arc discharge between two graphite electrodes was done in a stainless steel chamber that was filled with a mixture of hydrogen and helium at different proportions, without any catalyst. Soot materials containing graphene with web like appearance were formed.

1.1.5 Stability of graphene

Graphene is the two-dimensional counterpart of three dimensional graphite, exhibiting high crystal quality and ballistic conduction. But according to some earlier reports, perfect two-dimensional crystals cannot exist in free State [26-30]. This discrepancy can be resolved by considering the graphene structures studied so far to be an integral part of a larger three-dimensional structure, either supported by a substrate or embedded in a three dimensional matrix [31-33]. But surprisingly, individual graphene sheets (Figure 4) freely suspended on a micro fabricated scaffold in vacuum or in air have also been reported [34]. At first more than 70 years ago, Peierls [27, 28] and Landau [35,36] raised questions about the existence of a strictly two-dimensional (2D) crystal. They showed that in the standard harmonic approximation [37] thermal fluctuations destroy the long-range order which leads to the melting of 2D lattice at any finite temperature. Later, Mermin and Wagner proved that a magnetic long-range order could not exist in one and two dimensions [35] and later extended the proof to crystalline order in 2D [30]. Importantly, number of experiments on thin films were in agreement with the theory, showing that below a certain thickness, typically of dozens of atomic layers, the films segregate into islands or decompose unless they constitute an inherent part of a three-dimensional (3D) system [38, 39]. However, although the theory does not allow perfect crystals in 2D space, it does not forbid nearly perfect 2D crystals in 3D space. Indeed, a detailed analysis of the 2D crystal problem beyond the harmonic approximation has led to the conclusion [40-42] that the interaction between bending and of stretching long-wavelength phonons could in principle stabilize atomically thin membranes through their deformation in the third dimension [42].
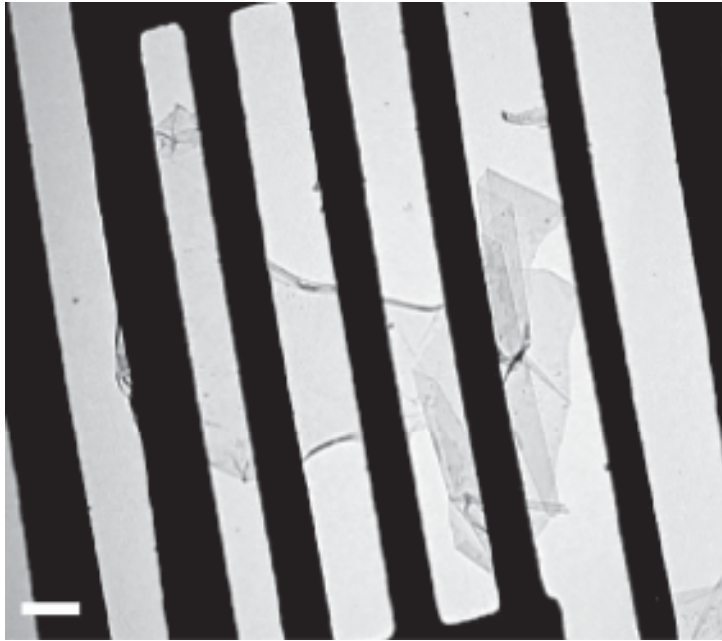
Figure 4. *TEM image of a suspended graphene membrane.*

(Scale bar, 500 nm) (From ref. [33]).

1.1.6 Electronic structure

Graphene honeycomb lattice is composed of two equivalent carbon sublattices A and B, Figure 5a and 5b shows the first Brillouin zone of graphene, with the high-symmetry points M, K, K' and Γ marked. Note that K and K' are two inequivalent points in the Brillouin zone. The s, p_x and p_y orbitals of carbon atoms form σ bonds with neighboring carbon atoms. The π electrons in the p_z orbital, one from each carbon, form the bonding π and the anti-bonding π* bands of graphene. Dispersion relation of these π-electrons is described by the tight binding model, incorporating only the first nearest neighbour interactions [Eq.(1)]: [43, 44]
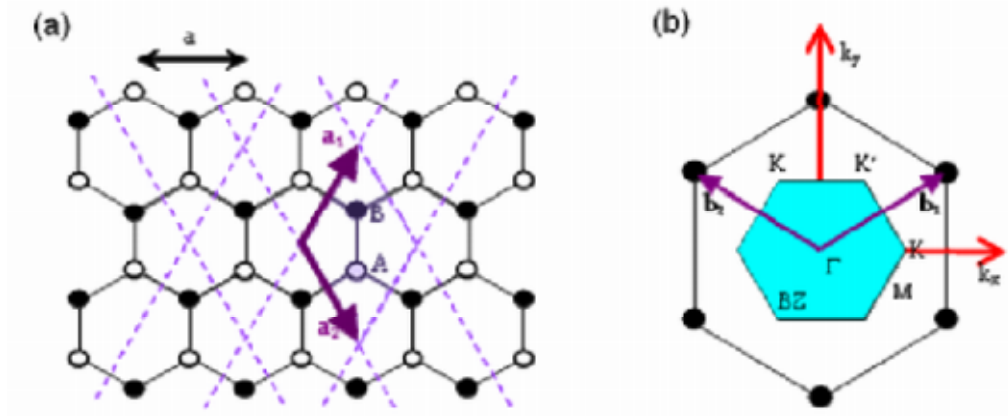
Figure 5 a) Graphene lattice. $\vec{a}_1$ and $\vec{a}_2$ are the unit vectors. (b) Reciprocal lattice of graphene. Shaded hexagon is the first Brillouin zone. $\vec{b}_1$ and $\vec{b}_2$ are reciprocal lattice vectors.

$$E^{\pm}(k_x, k_y) = \pm\gamma_0 \sqrt{1 + 4\cos\frac{\sqrt{3}k_x a}{2}\cos\frac{k_y a}{2} + 4\cos^2\frac{k_y a}{2}} \qquad \text{(1)}$$

where $a = \sqrt{3}a_{CC}$ is the carbon – carbon distance (1.42 Å) and γ_o, the transfer integral, is the matrix element between the π-orbitals of neighboring carbon atoms and its magnitude is ~ 3eV. The – sign in Eq.1 refers to the π-band which is fully occupied in graphene and the + sign corresponds to the totally empty anti-bonding π* band. The π and π* bands touch at the K and K′ points. A Taylor expansion of Eq.1 around K or K' points yield linear dispersion bands [Eq. (2)].

$$E^{\pm}(k) = \pm\gamma\left|\vec{k}\right| \qquad \text{(2)}$$

Here, $\vec{k}$ is measured with respect to the K-point, $\gamma = \hbar v_F = \sqrt{3}a\gamma_0 / 2$ and v_F is the

Fermi group velocity. The linear bands, a result of graphene's crystal symmetry, are a

hallmark of graphene giving rise to many of the interesting physical properties such as half -

integer quantum Hall effect, Berry's phase and Klein – paradox [45, 46]. Within the linear –

band approximation, the constant energy contours are circles around the K and K' points.

The effective Hamiltonian near the K-point can be expressed by the Dirac equation with zero

mass [Eq. (3)].

$$H = \begin{pmatrix} 0 & \gamma k \\ \gamma k & 0 \end{pmatrix} = \hbar v_F \, \vec{\sigma}.\vec{k}$$

(3)

Here $\vec{\sigma}$ is the 2d pseudospin Pauli matrix. Physically, this implies that the electronic states

near the K- point are composed of states belonging to different sub lattices A and B and their

relative contributions is taken into account using two component wave functions (spinors).

The eigen functions near K are given by Eq. (4)

$$\psi_{s,k}^{o}(\vec{r}) = \frac{1}{\sqrt{2}} \begin{pmatrix} 1 \\ se^{i\theta_k} \end{pmatrix} e^{i\vec{k}.\vec{r}}$$

(4)

Where s = ± 1 is the band index and $\theta_{\vec{k}}$ is the polar angle of the wave vector $\vec{k}$. Eq.4

reflects that the pseudospin vector is parallel to the wave vector $\vec{k}$ in the upper band (s = 1)

and is anti-parallel in the lower band (s = -1). The wave functions at K and K' are related by

time-reversal symmetry. The pseudospin and Berry phase may be manipulated by application

of an inhomogeneous lattice distortion. Interestingly, a non-constant lattice distortion can lead to a valley-Hall effect, analogous to the spin-Hall effect in semiconductors [47].

The electronic dispersion of bi-layer graphene is different from that of single-layer graphene. The lattice structure of a bi-layer graphene is shown in Figure 6 (a) and (b). Where the top and bottom layers are represented by solid and dashed lines, indexes 1 and 2 label the sublattices of the bottom and top layers, respectively. The A_2 sublattice of the top layer is exactly on top of the sublattice B_1 of the bottom layer. In addition to the in-plane nearest neighbour hopping energy γ_0 (A_1-B_1 or A_2-B_2), there is interlayer hopping energy γ_1 (A_2-B_1). Taking only these two energy scales and neglecting all other hopping energies (B_2-A_1, A_2-A_1 or B_2-B_1), the Hamiltonian of a bi-layer graphene near the K-point can be written as Eq. (5).

$$H = \begin{pmatrix} 0 & \gamma k & 0 & 0 \\ \gamma k & 0 & \gamma_1 & 0 \\ 0 & \gamma_1 & 0 & \gamma k \\ 0 & 0 & \gamma k & 0 \end{pmatrix}$$

(5)

The eigen values of this Hamiltonian are given by Eq. (6)

$$E_{sj}(k) = s\left[\left(\sqrt{\left(\frac{\gamma_1}{2}\right)^2 + (\gamma_0 k)^2}\right)(-1)^j \frac{\gamma_1}{2}\right]$$

(6)

where s = ± 1 is a band index, j is a sub band index (j = 1, 2). Figure 6c shows the electronic dispersion of the bi-layer, where γ_1 is the energy separation between the two sub-bands in

conduction or valence bands. There is no gap between the valence band and the conduction band. However, a gap can open on application of an electric field perpendicular to the bi-layer [48,49].
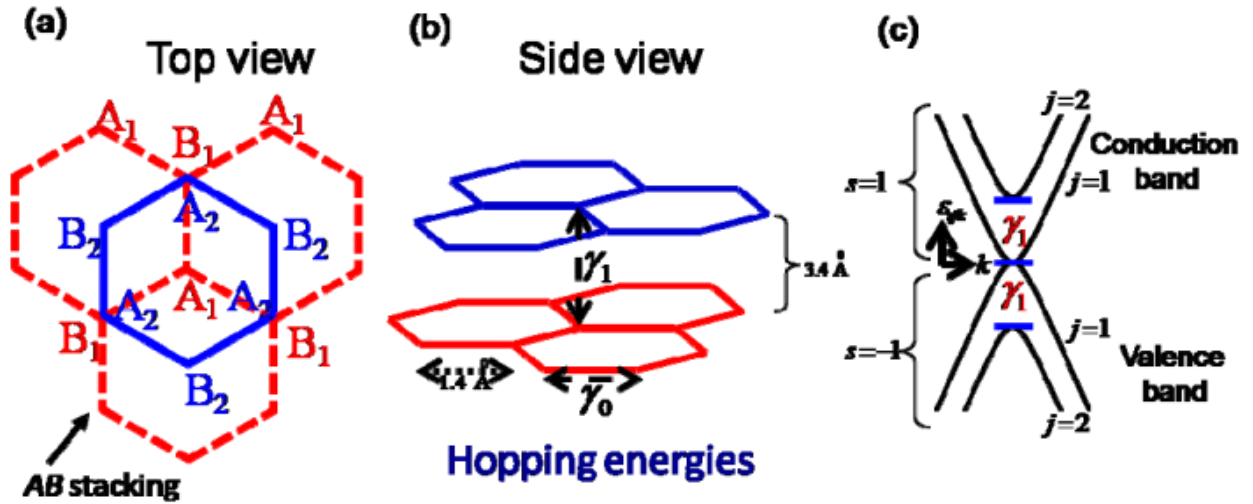
Figure 6. *(a) Top and (b) side view of a bi-layer graphene. A_1, B_1 are the sub lattices of the bottom layer and A_2, B_2 are sublattices of the top layer. c) Energy dispersion of a bi-layer graphene. Here γ_1 is the energy separation between the two sub bands.*

A band gap has been observed by angle-resolved photo-emission experiments on a chemically doped bi-layer graphene [31] where the electric field arises due to charge transfer from the dopants to the carbon atoms. A direct application of top-gate electric field to the back gated bi-layer field effect transistor gives a controlled way to manipulate the band gap, presenting a possibility of electrostatically controlled graphene-based devices [50].

1.1.7 Raman spectroscopy

Raman spectroscopy has emerged as an effective probe to characterize graphene sample in terms of the number of layers and their quality [51-59]. Single-layer graphene shows the well-known G-band characteristic of the sp^2 carbon network around 1580 cm^{-1}. The D band around 1350 cm^{-1} and D' band around 1620 cm^{-1} are defect induced. The 2D band at ~2680 cm^{-1} differs in single and few-layer graphene and can be understood on the basis of the double resonance Raman process involving different electronic dispersion [59-65]. The 2D band can be employed to determine the number of layers in few-layer graphene. By combining Raman experiments with *in-situ* transport measurements of graphene in field-effect transistor geometry, it has been shown that the G-modes of single- and bi-layer graphenes blue shift on doping with electron as well as holes [64-69]. On the other hand, the 2D band blue-shifts on hole doping whereas it red shifts on doping with electrons [70-74]. The relative intensity of the 2D band is quite sensitive to doping. Theoretical calculations based on time-dependant perturbation theory have been employed to explain the observed shifts of the G-band. Comparison between theory and experiment, however, is not entirely satisfactory at high doping levels ($>1\times10^{13}$/cm^2) and the disagreement is greater for the 2D band. In the case of bi-layer graphene, [75-78] the blue shift of the G-band with doping has contributions from phonon-induced inter-band and intra-band electronic transitions, thereby giving an experimental measure of the overlap integral between A and B atoms in the two layers. Furthermore, the in-plane vibration in bi-layer graphene splits into a symmetric Raman active mode (E_g) and an anti-symmetric infrared active mode (E_u). Doping dependence of these modes by Raman has been examined [79,80].

1.1.8 Graphane

Graphane is a "hypothetical" two-dimensional polymer of carbon and hydrogen with a hexagonal network. All the carbon atoms in graphene are sp^3 hybridized and the hydrogen atoms are bonded to carbon on both sides of the plane in an alternating manner. First principle density functional theory calculations show a binding energy comparable to other hydrocarbons such as benzene, cyclohexane and polyethylene.
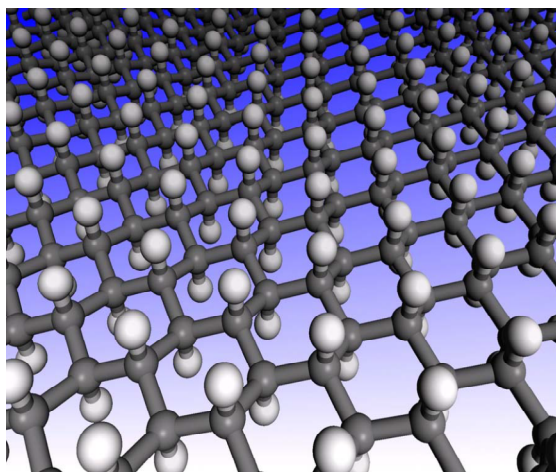
Figure 7. *Structure of graphane in the chair conformation. The carbon atoms are shown in gray and the hydrogen atoms in white. The figure shows the hexagonal network with carbon in the sp^3 hybridization. [From reference 77]*

Hydrocarbons are the simplest organic compounds made only of carbon and hydrogen [82, 83]. Some of them occur naturally in the form of crude oil and natural gas. Others are synthesized such as polyethylene and other plastics. They are readily oxidized to produce carbon dioxide and water with a considerable release of energy; therefore, they are usually good fuels. All known hydrocarbons, until now are the molecules that consist of a carbon

backbone with hydrogen atoms attached. The backbone can be a linear chain, a ring, or combinations of both. On the contrary, graphane is the first extended two-dimensional covalently bonded hydrocarbon. Graphane is predicted to be a semiconductor, because of its novel structure and low dimensionality. There is a fully fluorinated analog, poly-(carbon monofluoride) with formula CF, which has been synthesized earlier [84]. Because fluorine is known to replace hydrogen in many hydrocarbons, the existence of this fully fluorinated form gives further support to the prediction of this new academic material.

Graphane has two favorable conformations: a chair-like conformer with the hydrogen atoms alternating on both sides of the plane and a boat-like conformer with the hydrogen atoms alternating in pairs. In the chair conformer, every C-C bond connects carbon atoms with hydrogen attached at opposite sides of the plane (Figure 7). The calculated C-C bond length of 1.52 Å is similar to the sp^3 bond length of 1.53 Å in diamond and is much greater than 1.42 Å characteristic of sp^2 carbon in graphene. The boat conformer has two different types of C-C bonds: those connecting carbons bonded to hydrogen atoms on opposite sides of the plane with a bond length of 1.52 Å and those connecting carbon atoms bonded to hydrogen atoms on the same side of the plane with a bond length of 1.56 Å, slightly longer due to H-H repulsion [85]. The C-H bond length of 1.1 Å is similar in both conformers and typical of hydrocarbon compounds. The graphene bonds are fully saturated and there is no opportunity for hydrogen bonding between the sheets.

Experimentally, Sunmin Ryu *et al*. have shown the reaction of single-layer graphene with hydrogen atoms generates sp^3 C-H bonds on the basal plane and the reduced material gets dehydrogenated on photothermal heating [86]. In their experiments graphene samples coated with hydrogen silsesquioxane (HSQ) (30 nm thick) were irradiated with 30 keV electrons at various doses (0.5~8 mC/cm^2). In an approach, Elias *et al*. [87] have employed hydrogen plasma to hydrogenate graphene samples. In this process, graphene samples deposited on silicon substrate were exposed to cold hydrogen plasma ignited between two aluminum electrodes. During experiments, the samples were kept 30 cm away from the discharge zone in order to minimize any possible damage by energetic ions. It has also shown that the reaction with hydrogen is reversible, the original metallic state, the lattice spacing, and even the quantum Hall effect could be restored after annealing.

Recently, Rao *et al*. [88] showed that Birch-reduction of few-layer graphene gives rise to hydrogenated graphene containing up to 5 wt. % of hydrogen. Interestingly, hydrogenated graphene decomposes on heating up to 500 $^\circ$C or on laser irradiation, releasing all the hydrogen. This result demonstrates that the sp^3 C-H bond of hydrogenated graphene can be considered to act as a reversible chemical storage of hydrogen.

1.1.9 Graphene nanoribbons

Graphene nanoribbons, are strips of graphene with ultra-thin width (less than 50 nm). Depending on the width and edge configuration, graphene nanoribbons (GNRs) can be either metallic or semiconducting. Graphene nanoribbons with controlled widths were prepared by unzipping of nanotubes [Figure 8]
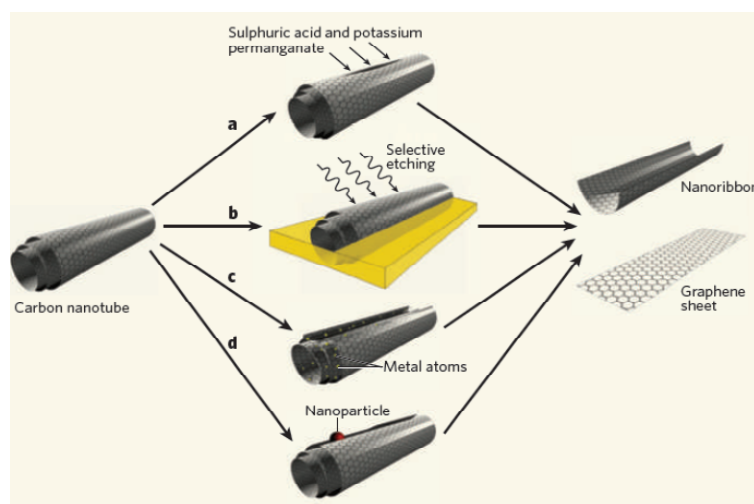
Figure 8. *Methods for unzipping carbon nanotubes. a) Unzipping of multiwalled carbon nanotubes by treating with sulphuric acid and potassium permanganate (an oxidizing agent) to form nanoribbons or graphene sheets. b) Argon plasma etching of nanotubes embedded polymer film. c) Insertion of alkali-metal atoms between the concentric cylinders of a multiwalled carbon nanotube, causes graphene sheets to peel off. d) A method still to be explored would use catalytic metal nanoparticles to cut along the length of a nanotube like a pair of scissors. [From reference 81]*

1.2 Applications

1.2.1 Batteries

Owing to its reversibility and reasonable specific capacity, graphite is generally employed as anode material in Li-ion batteries (Figure 9). However, new electrode materials with higher capacity and stability need to be developed for Li-ion batteries to achieve higher energy density and durability. Graphene has been considered as one of the promising anodic materials in Li-ion batteries, as it comprises good electrical conductivity, high surface area and chemical tolerance [89, 90]. Song *et al.* [91] have reported that graphene exhibits a relatively high reversible capacity of 672 mAhg^{-1} having much enhanced cycling performance relative to graphite. The capacity and cycle performance of Li-ion battery has been further improved using graphene based hybrid nanostructures as electrodes [92].

Figure 9. *Schematic illustration of synthesis and structure of SnO$_2$/graphene for battery application. [From reference 87]*

1.2.2 Composites

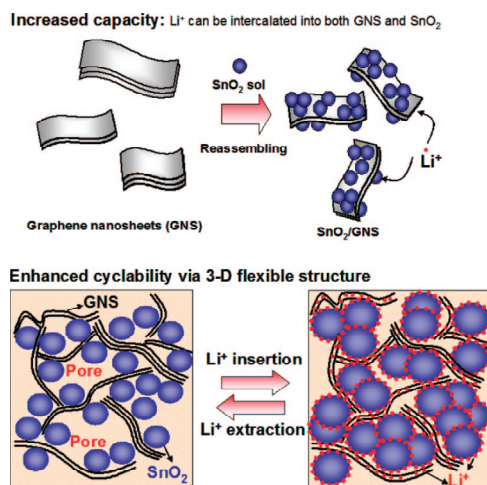Graphite is soft and flaky, and cannot be used in load-bearing structures. This problem could be solved by making a composite material of graphene sheets and polymers. The manufacturing of such composites requires not only that graphene sheets be produced on a sufficient scale but that they also be incorporated, and homogeneously distributed, into various matrices. Unfortunately, owing to their hydrophilic nature, graphene oxide sheets can only be dispersed in aqueous media that are incompatible with the most organic polymers. In addition, graphite oxide is electrically insulating, unlike graphite, which limits its usefulness for the synthesis of conductive nanocomposites. It has been demonstrated, [93, 94] however, that the electrical conductivity of graphite oxide can be significantly increased by chemical reduction, presumably owing to the restoration of a graphitic network of sp^2 bonds. Processing of nanographene platelets to produce composites has been briefly reviewed by Jang *et al*. [95]

Polyacrylonitrile nanofibers reinforced by graphite nanoplatelets have been prepared and have improved mechanical properties [96]. Hansma *et al*. [97] indicated how a combination of adhesives and high-strength structures such as graphene and carbon nanotubes can yield strong, light-weight and damage-resistant materials. Ramanathan *et al*. [98] reported that 1 wt% of functionalized graphene sheets in poly(acrylonitrile) increases the glass transition temperature (T_g) of the polymer by over 40 ºC and an increase of nearly 30 ºC is observed with only 0.05 wt% of graphene in poly(methyl methacrylate) (PMMA). An addition of approximately 1 wt% of graphene to PMMA leads to an increase in the elastic modulus by 80% and in the ultimate tensile strength by 20%. A comparative study by these workers

shows that among all the nano-filler materials considered, single-layer functionalized graphene gives the best results. Das *et al.* [99] have studied the mechanical properties of polyvinyl alcohol (PVA) and PMMA composites reinforced by functionalized few-layer graphene by employing the nanoindentation technique. The addition of 0.6 wt% of the graphene results in a significant increase in both the elastic modulus and hardness. The crystallinity of PVA also increases with the addition of few-layer graphene. An observed improvement in the mechanical properties of the polymers is suggested to have arisen from the good mechanical interaction between the polymer and the few-layer graphene, which in turn, provides better load-transfer between the matrix and the graphene. Epoxy composites of few-layer graphene show very interesting properties which are useful for the development of thermal interface materials for electronic packaging and advanced composites [100]. A loading of nearly 25 vol % of graphene into epoxy matrix enhances the thermal conductivity by more than 3000 times. This surpasses the performance of conventional fillers that require a loading of nearly 70 vol % to achieve the same thermal conductivity.

1.2.3 Sensors

In many applications, solid-state gas sensors have been widely employed due to their high sensitivity, low production costs and miniature sizes [101,102]. Recently gas sensors using carbon nanotubes and semiconductor nanowires have also been demonstrated [103, 104]. The ultimate goal of any detection method is to attain the level of sensing even single atom or molecule. Such resolution has so far been beyond the reach of any detection technique, including solid-state gas sensors known for their exceptional sensitivity. The main reason for the limitation is fluctuations due to thermal motion of charges and defects, [105]

which leads to intrinsic noise exceeding the sought-after signal from individual molecules, usually by many orders of magnitude. But the micrometer-size sensors made from graphene are capable of detecting even individual molecules. Such gas sensors rely on the change in their electrical conductivity [106]. The observed change in conductivity arises due to a change in the carrier concentration of graphene, caused by adsorbed gaseous molecules acting as donors or acceptors. Some interesting properties of graphene render its sensitivity up to single atom or molecule level detection. First, as graphene is a two-dimensional (2D) material all carbon atoms in the plane are exposed to the analyte of interest [107]. Second, graphene is highly conductive with low Johnson noise (electronic noise generated by the thermal agitation of the charge carriers inside an electrical conductor at equilibrium, which happens irrespective of any applied voltage), therefore a little change in carrier concentration can cause a marked variation in electrical conductivity [107]. Third, graphene has very few crystal defects, [108] ensuring a low level of noise caused by thermal switching. Finally, four-probe measurements can be made on a single-crystal graphene device with ohmic electrical contacts having low resistance [107]. All these features contribute to maximize the signal-to-noise ratio to a level sufficient for detecting changes in a local concentration by less than one electron charge, e, at room temperature.

Ghosh *et al.* [109] have studied the sensor characteristics of thick films made of few-layer graphenes for NO_2, H_2O and aliphatic alcohols. Good sensitivities were observed for NO_2 and H_2O, and the sensitivity was mainly found to be affected by boron or nitrogen doping. Gas-sensing properties of graphene sheets deposited on $LiTaO_3$ substrates [110] as well as glucose sensors based on graphene have been reported [111, 112]. With glucose

oxidase (GOD) as an enzyme model, Shan *et al*. [112] constructed a novel polyvinylpyrrolidone protected graphene/polyethylenimine-functionalized ionic liquid/GOD electrochemical biosensor. Through the sensor, they reported direct electron transfer of GOD, demonstrating graphene's potential application for fabrication of glucose sensors. A linear response up to 14 mM of glucose was observed by them [112]. The possibilities of single-layer graphene to act as a mass sensor and an atomic dust detector have also been indicated [113].

Graphene chemically modified by electrodeposition of Pd nanoparticles [114], has been reported to show good response for H_2 sensing, as Pd has good affinity towards H_2. DFT calculations show that aluminum-doped graphene strongly chemisorbs CO molecules, forming Al-CO bonds. Thus, aluminum-doped graphene is expected to be a potential candidate for the detection of CO [115]. Chemically modified graphene has been used in bioelectronics as a sensor at both the microbial and the molecular level [116]. It acts as an interface to recognize single bacteria, a label-free, reversible DNA detector, and a polarity specific molecular transistor for protein/DNA adsorption.

References

1. L. Pauling, The Nature of the Chemical Bond, Cornell University Press, Ithaca, NY, 1960.

2. R. F. Curl, Rev. Mod. Phys. 1997 (69) 691.

3. H. Kroto, Rev. Mod. Phys. 1997 (69) 703.

4. R. E. Smalley, Rev. Mod. Phys. 1997 (69) 723.

5. S. Iijima, Nature 1991 (351) 56.

6. P. R. Wallace, Phys. Rev. 1947 (71) 622.

7. H.P. Boehm, Angew. Chem. Int. Ed. 2010 (49) 9332.

8. A. J. van Bommel, J. E. Crombeen, A. van Tooren, Surf. Sci. 1975 (48) 463.

9. X. Lu, M. Yu, H. Huang, R. S. Ruoff, Nanotechnology 1999 (10) 269.

10. C. Roscoe, J. M. Thomas, Proc. R. Soc. London Ser. A 1967 (297) 397.

11. K. S. Novoselov, A. K. Geim, S. V. Morozov, D. Jiang, Y. Zhang, S. V. Dubonos, I. V. Grigorieva, A. A. Firsov, Science 2004 (306) 666.

12. K. S. Novoselov, A. K. Geim, S. V. Morozov, D. Jiang, M. I. Katsnelson, I. V. Grigorieva, S. V. Dubonos, A. A. Firsov, Nature 2005 (438) 197

13. C. N. R. Rao, A. K. Sood, K. S. Subrahmanyam, A. Govindaraj, Angew. Chem. Int. Edition, 2009 (48) 7752.

14. A. K. Geim, K. S. Novoselov, Nat. Mater. 2007 (6) 183.

15. P. Blake, E. W. Hill, A. H. Casrto Neto, K. S. Novoselov, D. Jiang, R. Yang, T. J. Booth, A. K. Geim, Appl. Phys. Lett. 2007 (91) 063124.

16. B. Partoens, F. M. Peeters, Phys. Rev. B 2006 (74) 075404.

17. V. C. Tung, M. J. Allen and Y. Yang, Nat. Nanotec., 2009 (4) 25.

18. C. Berger, J. Phys. Chem., B, 2004 (108) 19912.

19. C. Berger, Z. M. Song, and X. B. Li, Science, 2006 (312) 1191.

20. C. G. Jernigan, B. L. Van Mil and J. L. Tedesco, Nano Lett, 2009 (9) 2605.

21. K. S. Kim, Y. Zhao and H. Jang, Nature, 2009 (457) 706.

22. A. Reina, X. T. Jia and J. Ho, Nano Lett, 2009 (9) 30.

23. X. S. Li, W. W. Cai and J. An, Science, 2009 (324) 1312.

24. K. S. Subrahmanyam, L. S. Panchakarla, A. Govindaraj and C. N. R. Rao, J. Phys. Chem. C. 2009 (113) 4257;

25. K. S. Novoselov, D. Jiang, F. Schedin, T. J. Booth, V. V. Khotkevich, S. V. Morozov, A. K. Geim, Proc. Natl Acad. Sci. USA, 2005 (102) 10451.

26.   R. E. Peierls, Helv. Phys. Acta 1934 (7) 81.

27.   R. E. Peierls, Ann. Inst. Henri Poincare 1935 (5) 177.

28.   L. D. Landau, Phys. Z. Sowjetunion 1937 (11) 26.

29.   N. D. Mermin, Phys. Rev. 1968 (176) 250.

30.   C. Berger, Z. Song, X. Li, X. Wu, N. Brown, C. Naud, D. Mayou, T. Li, J. Hass, A. N. Marchenkov, E. H. Conrad, P. N. First, W. A. de Heer, Science 2006 (312) 1191.

31.   T. Ohta, A. Bostwick, T. Seyller, K. Horn, E. Rotenberg, Science 2006 (313) 951.

32.   S. Stankovich, D. A. Dikin, G. H. B. Dommett, K. M. Kohlhaas, E. J. Zimney, E. A. Stach, R. D. Piner, S. T. Nguyen, R. S. Ruoff, Nature 2006 (442) 282.

33.   J. C. Meyer, A. K. Geim, M. I. Katsnelson, K. S. Novoselov, T. J. Booth, S. Roth, Nature 2007 (446) 60.

34. .   D. Landau, E. M. Lifshitz, Statistical Physics Part I, Pergamon, Oxford, 1980.

35.   L. D. Landau, Zur Theorie der Phasenumwandlungen II. Phys. Z., Vol. 11, Sowjetunion 1937.

36.   M. Born, K. Huang, Dynamical Theory of Crystal Lattices, Clarendon, Oxford, 1954.

37.   A. Venables, G. D. T. Spiller, M. Hanbucken, Rep. Prog. Phys. 1984 (47) 399.

38.   L. D. Landau, Phys. Z. Sowjetunion 1937 (11) 26.

39.   J. W. Evans, P. A. Thiel, M. C. Bartelt, Surf. Sci. Rep. 2006 (1) 61.

40. D. R. Nelson, L. Peliti, J. Physique 1987 (48) 1085.

41. Le Doussal, L. Radzihovsky, Phys. Rev. Lett. 1992 (69) 1209.

42. D. R. Nelson, T. Piran, S. Weinberg, Statistical Mechanics of Membranes and Surfaces, World Scientific, Singapore, 2004.

43. R. Saito, G. Dresselhaus, M. S. Dresselhaus, Physical Properties of Carbon Nanotubes, Imperial College Press, London, 1998.

44. A. H. Castro Neto, F. Guinea, N. M. R. Peres, K. S. Novoselov, A. K. Geim, Rev. Mod. Phys. 2009 (81) 109.

45. M. I. Katsnelson, K. S. Novoselov, A. K. Geim, Nat. Phys. 2006 (2) 620.

46. M. I. Katsnelson, Mater. Today 2007 (10) 20.

47. P. Gosselin, A. Bérard, H. Mohrbach, S. Ghosh, Eur. Phys. J. C 2009 (59) 883.

48. E. McCann, V. I. Fal'ko, Phys. Rev. Lett. 2006 (96) 086805.

49. H. Min, B. Sahu, S. K. Banerjee, A. H. MacDonald, Phys. Rev. B 2007 (75) 155115.

50. J. B. Oostinga, H. B. Heersche, X. Liu, A. F. Morpurgo, L. M. K. Vandersypen, Nat. Mater. 2008 (7) 151.

51. K. S. Novoselov, A. K. Geim, S. V. Morozov, D. Jiang, M. I. Katsnelson, I. V. Grigorieva, S. V. Dubonos, A. A. Firsov, Nature 2005 (438) 197.

52. Y. Zhang, J. W. Tan, H. L. Stormer, P. Kim, Nature 2005 (438) 201.

53. Z. Jiang, Y. Zhang, Y. W. Tan, H. L. Stormer, P. Kim, Solid State Commun. 2007 (143) 14.

54. K. S. Novoselov, Z. Jiang, Y. Zhang, S. V. Morozov, H. L. Stormer, U. Zeitler, J. C. Maan, G. S. Boebinger, P. Kim, A. K. Geim, Science 2007 (315) 1379.

55. K. S. Novoselov, E. McCann, S. V. Morozov, V. I. Fal'ko, M. I. Katsnelson, U. Zeitler, D. Jiang, F. Schedin, A. K. Geim, Nat. Phys. 2006 (2) 177.

56. E. V. Castro, K. S. Novoselov, S. V. Morozov, N. M. R. Peres, J. M. B. Lopes dos Santos, J. Nilsson, F. Guinea, A. K. Geim, A. H. Castro Neto, Phys. Rev. Lett. 2007 (99) 216802.

57. S. Reich, C. Thomsen, Philosophical Transactions of the Royal Society a-Mathematical Physical and Engineering Sciences 2004 (362) 2271.

58. J.-A. Yan, W. Y. Ruan, M. Y. Chou, Phys. Rev. B 2008 (77) 125401.

59. S. K. Saha, U. V. Waghmare, H. R. Krishnamurthy, A. K. Sood, Phys. Rev. B 2008 (78) 165421.

60. S. Piscanec, M. Lazzeri, J. Robertson, A. C. Ferrari, F. Mauri, Phys. Rev. B 2007 (75) 035427.

61. O. Dubay, G. Kresse, Phys. Rev. B 2003 (67) 035401.

62. M. Lazzeri, F. Mauri, Phys. Rev. Lett. 2006 (97) 266407.

63. C. H. Park, F. Giustino, M. L. Cohen, S. G. Louie, Nano Lett. 2008 (8) 4229.

64. W. Kohn, Phys. Rev. Lett. 1959 (2) 393.

65. A. Gupta, G. Chen, P. Joshi, S. Tadigadapa, P. C. Eklund, Nano Lett. 2006 (6) 2667.

66. A. C. Ferrari, Solid State Commun. 2007 (143) 47.

67.   A. C. Ferrari, J. C. Meyer, V. Scardaci, C. Casiraghi, M. Lazzeri, F. Mauri, S. Piscanec, D. Jiang, K. S. Novoselov, S. Roth, A. K. Geim, Phys. Rev. Lett. 2006 (97) 187401.

68.   M. A. Pimenta, G. Dresselhaus, M. S. Dresselhaus, L. G. Cancado, A. Jorio, R. Saito,Phys. Chem. Chem. Phys. 2007 (9) 1276.

69.   D. Graf, F. Molitor, K. Ensslin, C. Stampfer, A. Jungen, C. Hierold, L. Wirtz, Nano. Lett. 2007 (7) 238.

70.   A. Das, B. Chakraborty, A. Sood, Bull. Mater. Sci. 2008 (31) 579.

71.   Z. Ni, Y. Wang, T. Yu, Z. Shen, Nano Res. 2008 (1) 273.

72.   D. M. Basko, Phys. Rev. B 2008 (78) 125418.

73.   D. M. Basko, Phys. Rev. B 2007 (76) 081405.

74.   Y. You, Z. Ni, T. Yu, Z. Shen, Appl. Phy. Lett. 2008 (93) 163112.

75.   Y. Zhang, J. W. Tan, H. L. Stormer, P. Kim, Nature 2005 (438) 201.

76.   J. Rohrl, M. Hundhausen, K. V. Emtsev, T. Seyller, R. Graupner, L. Ley, Appl. Phy. Lett. 2008 (92) 201918.

77.   N. Ferralis, R. Maboudian, C. Carraro, Phys. Rev. Lett. 2008 (101) 156801.

78.   Z. H. Ni, H. M. Wang, Y. Ma, J. Kasim, Y. H. Wu, Z. X. Shen, ACS Nano 2008 (2) 1033.

79.   T. Yu, Z. H. Ni, C. L. Du, Y. M. You, Y. Y. Wang, Z. X. Shen, J. Phys. Chem. C. 2008 (112) 12602.

80.   T. M. G. Mohiuddin, A. Lombardo, R. R. Nair, A. Bonetti, G. Savini, R. Jalil, N.Bonini, D. M. Basko, C. Galiotis, N. Marzari, K. S. Novoselov, A. K. Geim, A. C. Ferrari, Phys. Rev. B 2009 (79) 205433.

81.   M. Terrones, Nature 2009 (458) 845.

82.   S. Guo, S. Dong, Chem. Soc. Rev. 2011 (40) 2644.

83.   G. A. Olah, Á. Molnár, Hydrocarbon Chemistry, Wiley-Interscience, Hoboken, NJ, USA, 2003.

84.   N. Watanabe, T. Nakajima, H. Touhara, Graphite fluorides Elsevier, Amsterdam, 1988.

85.   J. O. Sofo, A. S. Chaudhari, G. D. Barber, Phys. Rev. B 2007 (75) 153401.

86.   S. Ryu, M. Y. Han, J. Maultzsch, T. F. Heinz, P. Kim, M. L. Steigerwald, L. E. Brus, Nano Lett. 2008 (8) 4597.

87.   D. C. Elias, R. R. Nair, T. M. G. Mohiuddin, S. V. Morozov, P. Blake, M. P. Halsall, A. C. Ferrari, D. W. Boukhvalov, M. I. Katsnelson, A. K. Geim, K. S. Novoselov, Science 2009 (323) 610.

88.   K. S. Subrahmanyam, P. Kumar, U. Maitra, A. Govindaraj, K. P. S. S. Hembram, U. V. Waghmare and C. N. R. Rao, Proc. Natl. Acad. Sci., 2011 (108) 2674.

89.   X. Wang, L. J. Zhi, K. Mullen, Nano Lett. 2008 (8) 323.

90.   S. Gilje, S. Han, M. Wang, K. L. Wang, R. B. Kaner, Nano Lett. 2007 (7) 3394.

91.   P. Guo, H. Song, X. Chen, Electrochem.Commun. 2009 (11) 1320.

92.   S. M. Paek, E. Yoo, I. Honma, Nano Lett. 2009 (9) 72.

93.   S. Stankovich, R. D. Piner, X. Q. Chen, N. Q. Wu, S. T. Nguyen, R. S. Ruoff, J. Mater. Chem. 2006 (16) 155.

94.   N. A. Kotov, I. Dekany, J. H. Fendler, Adv. Mater. 1996 (8) 637.

95.   J. Lu, L. T. Drzal, R. M. Worden, I. Lee, Chem. Mater. 2007 (19) 6240.

96.   J. J. Mack, L. M. Viculis, A. Ali, R. Luoh, G. Yang, H. T. Hahn, F. K. Ko, R. B. Kaner, Adv. Mater. 2005 (17) 77.

97.   P K Hansma, P. J. Turner, R. S. Ruoff, Nanotechnology 2007 (18) 044026.

98.   T. Ramanathan, A. A. Abdala, StankovichS, D. A. Dikin, M. Herrera Alonso, R. D. Piner, D. H. Adamson, H. C. Schniepp, ChenX, R. S. Ruoff, S. T. Nguyen, I. A. Aksay, R. K. Prud'Homme, L. C. Brinson, Nat. Nanotechnol. 2008 (3) 327.

99.   B. Das, K. Eswar Prasad, U. Ramamurty, C. N. R. Rao, Nanotechnology 2009 (20) 125705.

100.   Yu, P. Ramesh, M. E. Itkis, E. Bekyarova, R. C. Haddon, J. Phys. Chem. C 2007 (111) 7565.

101.   P. T. Moseley, Meas. Sci. Technol. 1997 (8) 223.

102.   S. Capone, J. Optoelect. Adv. Mater. 2003 (5) 1335.

103.   C. X. Cong, T. Yu, Z. H. Ni, L. Liu, Z. X. Shen, W. Huang, J. Phys. Chem. C 2009 (113) 6529.

104.   P. G. Collins, K. Bradley, M. Ishigami, A. Zettl, Science 2000 (287) 1801.

105.   P. Dutta, P. M. Horn, Rev. Mod. Phys. 1981 (53) 497.

106.   C. Lee, X. Wei, J. W. Kysar, J. Hone, Science 2008 (321) 385.

107.   F. Schedin, A. K. Geim, S. V. Morozov, E. W. Hill, P. Blake, M. I. Katsnelson, K. S. Novoselov, Nat. Mater. 2007 (6) 652.

108.   K. S. Nonoselov, E. McCann, S. V. Morozov, V. I. Fal'ko, M. I. Katsnelson, U.Zeitler, D. Jiang, F. Schedin, A. K. Geim, Nat. Phys. 2006 (2) 177.

109.   A. Ghosh, D. J. Late, L. S. Panchakarla, A. Govindaraj, C. N. R. Rao, J. Exp. Nanosci. 2009 (4) 313.

110.   R. Arsat, M. Breedon, M. Shafiei, P. G. Spizziri, S. Gilje, R. B. Kaner, K. Kalantarzadeh, W. Wlodarski, Chem. Phys.Lett. 2009 (467) 344.

111.   J. Lu, I. Do, L. T. Drzal, R. M. Worden, I. Lee, ACS Nano 2008 (2) 1825.

112.   C. Shan, H. Yang, J. Song, D. Han, A. Ivaska, L. Niu, Anal. Chem. 2009 (81) 2378.

113.   A. Sakhaee-Pour, M. T. Ahmadian, A. Vafai, Solid State Commun. 2008 (145) 168.

114.   R. S. Sundaram, C. Gómez-Navarro, K. Balasubramanian, M. Burghard, K. Kern, Adv. Mater. 2008 (20) 3050.

115.   Z. M. Ao, J. Yang, S. Li, Q. Jiang, Chem. Phys.Lett. 2008 (461) 276.

116.   N. Mohanty, V. Berry, Nano Lett. 2008 (8) 4469.

CHAPTER 2

GRAPHENE-METAL OXIDE COMPOSITES[*]

2.1 Chemically bonded ceramic oxide coatings on graphene

Summary

In this chapter we describe the synthesis of graphene-metal oxide composites in which graphene chemically bonded to metal oxide. It involves the reaction of functionalized graphene with metal halides such has TiCl4, $AlCl_4$ etc... followed by hydrolysis and calcination. The thickness of oxide layer being controlled by the number of cycles of reaction with metal halide and H_2O. After calcining graphene-metal oxide composite, we have been able to prepare thin films of metal oxide.

2.1.1 Introduction

After the discovery of graphene [1-4], there has been considerable research in the area of two dimensional materials, many of which are based on inorganic layered compounds [5-7]. Several researchers have prepared the composites of these materials and studied their properties [8, 9]. An aspect of particular interest pertains to coat thin layers of metal oxides on the graphene surfaces to prepare functional composites. Such composites may indeed possess valuable properties, specially if the oxide layers are chemically bonded to graphene [10]. Knowing that metal-oxygen bonds can be formed with substrates by the reaction of appropriate chloro-compound with the hydroxyl groups present on the substrate, we have explored whether ceramic oxide-coated nanostructures can be obtained by the reaction of reactive metal chlorides with oxygenated graphene. This seemed entirely feasible since the oxygenated graphene surface possess surface hydroxyl and carboxyl groups on the surface. The surface functional groups on reaction with vapor of metal halide, such has $TiCl_4$ can form metal-oxygen bonds by eliminating HCl leaving extra metal-chlorine bonds. The metal-chlorine bonds can be hydrolyzed by treatment with water vapor and the hydroxide layer again reacted with metal chloride. On repeating the process several times followed by calcination, we have obtained graphene with a chemically-bonded ceramic oxide coating of the desired thickness. By calcining the composite, we obtain free-standing oxide nano-films. Miyauchi and co-workers have employed carbon nanotubes as template for the preparation of nanotubes and nanowires of inorganic materials, specially of metal oxides [11]. For this purpose, the CNTs were covered with an oxide precursor or a gel and the nanotube burnt off

in air. Thin films of metal oxides possess superior properties [12]. We illustrate the process schematically in Figure 1.
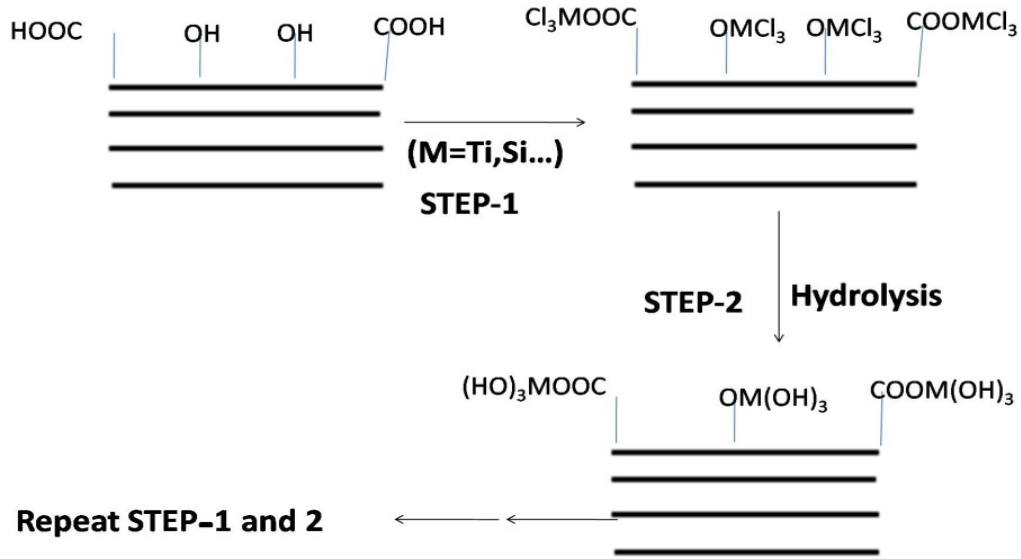

Figure 1. *The ceramic oxide coating process for functionalized graphene.*

2.1.2. Experimental methods

Graphite oxide (GO) was synthesized by the modified Hummer's method [13]. Graphene samples were obtained from graphite oxide by the thermal exfoliation [EG] in a furnace preheated to 250 °C. Figure 2, shows the schematic diagram of experimental set-up used for coating metal oxides on to graphene [14]. It consists of three glass chambers, one to contain the metal halide ($TiCl_4$, $SiCl_4$, etc), the second for graphene and the third for water. High-vacuum stopcocks interconnect the chambers, which are connected to a vacuum pump. In a typical preparation, the sample chamber is evacuated for 15 min and the metal halide vapor from first chamber is allowed to enter the reaction chamber and allowed to react for

10 min. The unreacted metal halide vapor is removed by evacuation. In this step, the metal halide reacts with the oxygen functionalities on graphene giving out HCl. Water vapor from the third chamber is then passed on to the sample chamber for hydrolyzing the remaining unreacted chlorines of the metal halide. These two procedures are repeated several times. The graphene samples so obtained were heated to 350 °C to produce metal oxide coatings. In the case of TiO_2, the samples obtained after calcination at 350 °C and 600 °C for 12 h are designated as G-TiO_2-350 and G-TiO_2-600 respectively. The sample is heated to 600 °C to burns off the carbon giving only a thin free-standing film of TiO_2. It should be noted that coating obtained on the graphene would not be of the oxide at room temperature, but of the same oxidic/hydroxidic species. It is only after the calcination that an oxide coating was forms. For purpose of brevity, we have called the products obtained at room temperature as oxide coated nanostructures.
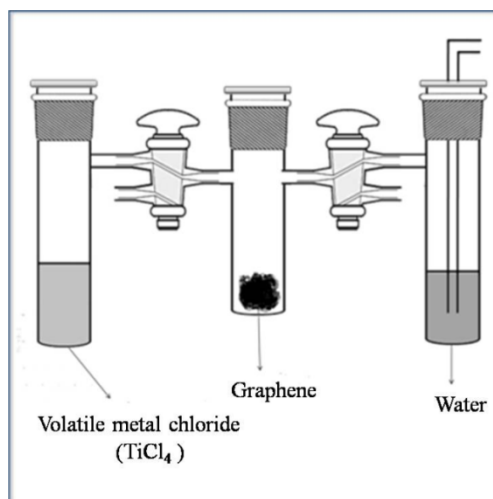

Figure 2. *Schematic diagram of the experimental set-up.*

X-ray diffraction (XRD) patterns were recorded with Cu-Kα radiation using a Rich-Siefert XRD-300-TT diffractometer. Scanning electron microscope (SEM) images were recorded with a FEI NOVA NANOSEM 600. Transmission electron microscope (TEM) images were obtained with a JEOL TEM 3010 instrument fitted with a Gatan CCD camera operating at an accelerating voltage of 300 kV. Samples for TEM analysis were prepared by dispersing the product in ethanol. A drop of the suspension was then put it on a holey carbon grid and allowed to evaporate. Atomic force microscope (AFM) measurements were performed using an Innova atomic microscope.
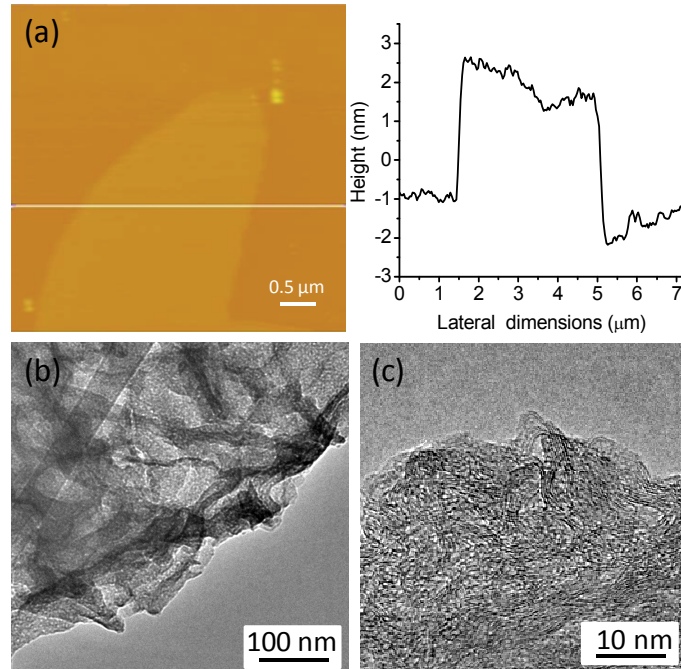

Figure 3. *(a) AFM image of graphene exfoliated at 250 ^{o}C,*

(b, c) TEM image of the same sample

AFM image of graphene exfoliated at 250 ^{o}C is shown in Figure 3a. Cross section analysis indicates a height of 3 nm for EG which corresponds to 8-9 layers of graphene.

In figure 4, we show IR spectra of GO and EG. GO shows broad band around 3400 cm^{-1} corresponds to –OH stretching and 1730 cm^{-1} corresponding to C=O stretching of carboxylic group. In EG we observed band due to C=O from carboxylic acid with reduced intensity.
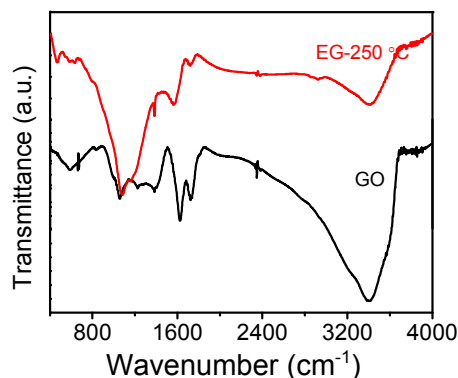

Figure 4. *IR spectra of GO and EG*

2.1.3. Results and discussion

The method employed by us to prepare graphene chemically bonded to metal oxide films, by employing the experimental set-up shown in Figure 1, gives rise to M-O-C bonds. For our present work graphitic oxide was synthesized by modified hummers method which was exfoliated around 250 ^{O}C (EG) to ensure enough functional groups are there on graphene surface to react chemically with metal halides (TiCl$_4$, SiCl$_4$), which is in vapor phase. Reaction with water vapor results in the hydrolysis of the unreacted chloride, which on calcination gives oxidic species. Thus, in the case of TiCl$_4$ we obtain a coating of a TiO$_2$ film on graphene by this means. The thickness of the oxide layer depends on the number of times we carry out the reaction with the metal halide. In Figure 5, we show FESEM images of TiO$_2$ chemically bonded to graphene (G-TiO$_2$) obtained after the reaction of TiCl$_4$ with graphene

at room temperature and subjected to calcination at different temperatures. The energy-dispersive X-ray analysis (EDX) pattern given in the inset of the Figure 5a shows the presence of Ti, O and Cl in the sample prepared at room temperature. Chlorine is absent on heating to 350 °C. The SEM image (Figure 5b) of G-TiO$_2$ heated at 350 °C (G-TiO$_2$-350) for 12 h gives nanosheets of TiO$_2$ on graphene. An EDX pattern (see inset of Figure 5b shows the presence of only Ti and O, and does not show any chlorine. In Figures 6a and b, we show TEM images of G-TiO$_2$ obtained at room temperature and at 350 °C respectively. On calcining the TiO$_2$-bonded graphene composite at 600 °C for 12 h (G-TiO$_2$-600), the graphene sheets get oxidized, yielding TiO$_2$ nanosheets as shown by the SEM and TEM images in Figures 5c and 6c respectively. The EDX pattern (inset of Figure 5c) of the calcined sample confirms the presence of Ti and O. There is no carbon peak in 600 °C calcined sample; it shows TiO$_2$ sheets obtained are composed of only Ti and O.
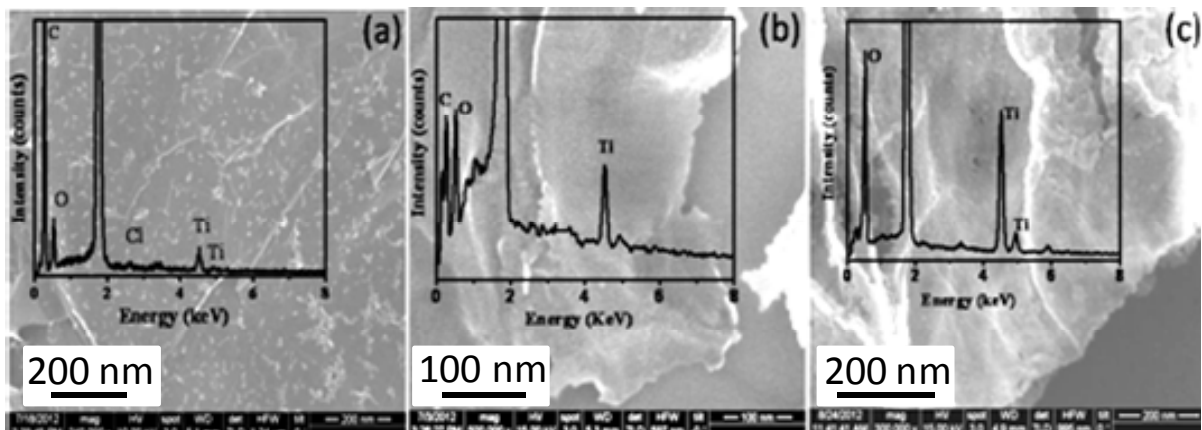

Figure 5. *SEM images (a) of TiO$_2$-bonded graphene prepared at room temperature, (b) of the same sample after calcination at 350 °C and (c) of TiO$_2$ nanosheets after the removal of graphene at 600 °C. Insets show EDX patterns.*
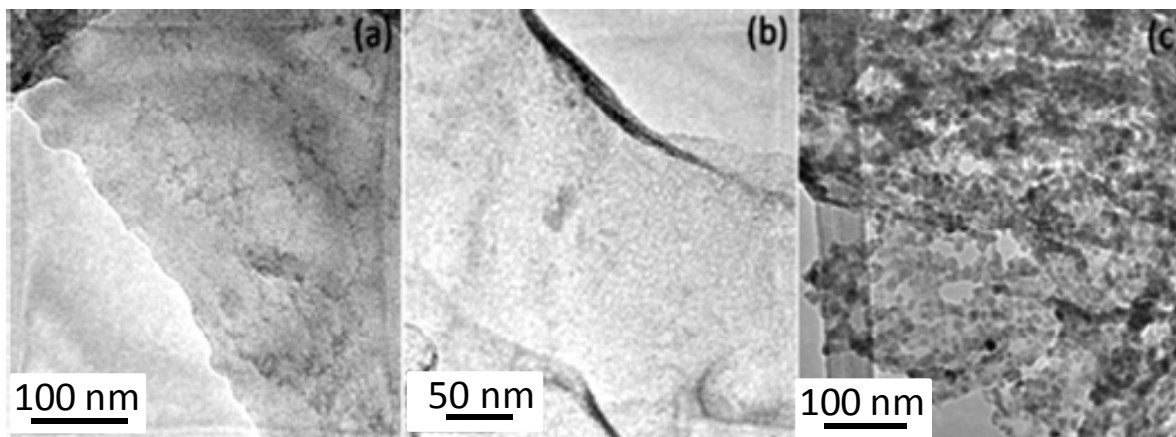
Figure 6. *TEM images (a) of TiO₂-bonded graphene prepared at room temperature,*

> *(b) The same sample after calcination at 350 ℃ and (c) of TiO₂ nanosheets*

> *after removal of graphene at 600 ℃.*

The XRD patterns in Figure 7 reveal the formation of TiO_2 in the anatase phase (a=3.785 A°, c=9.514 A°) after calcination at 600 ^{o}C for 12 h. The sample coated at room temperature was found to be amorphous.
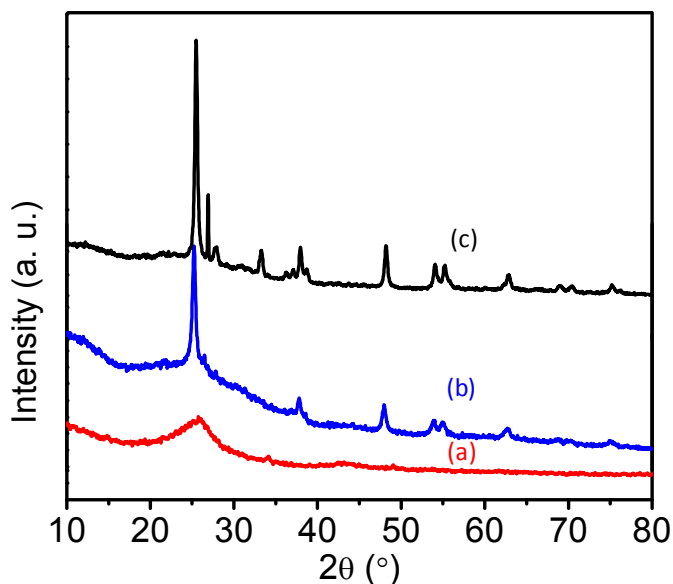

Figure 7. *XRD pattern of (a) graphene exfoliated at 250 ^{o}C, (b) the TiO₂ coated on graphene after calcination at 350 ℃ and (c) of TiO₂ nanosheets after removal of graphene at 600 ℃.*

Raman spectroscopy is a useful tool to characterize graphene and its composites. Single layer graphene shows well known G-band around 1570 cm^{-1} and a band around 1620 cm^{-1} (D'). The D' band is defect induced and not found in graphite. The D-band around 1350 cm^{-1} arising from disorder is very weak in a single layer graphene. The 2D band (2600 cm^{-1}) which appear in single layer graphene which is also sensitive to the number of layers and shows a greater structure (often a doublet). Room temperature coated sample shows no Raman peaks correspond to TiO_2 which indicates coating is amorphous (Figure 8).

Appearance of 2D-band in the G-TiO_2-350 composites indicates decrease in number of layers in compared to EG. G-TiO_2-600 calcined sample shows the absence of G and D band which confirms complete removal of carbon after calcining the sample at 600 ^{o}C. The TiO_2 obtained after calcination shows Raman peaks corresponding to anatase phase which is shown in below Figure 8.

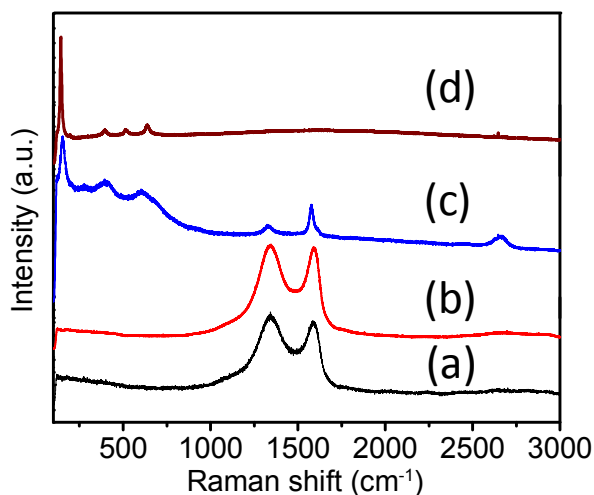**Figure 8.** *Raman spectra of (a) graphene exfoliated at 250 ^{o}C, (b) the same sample coated with TiO_2 at room temperature (b) after calcination at 350 ^{o}C and (c) of TiO_2 nanosheets after removal of graphene at 600 ^{o}C.*

The AFM image of G-TiO$_2$-350 shown in Figure 9a was obtained by the calcination of the composite at 350 °C corresponding to the graphene sheets covered with TiO$_2$ which is having thickness of ~ 1.5 nm. We could observe that graphene sheets are completely covered with TiO$_2$ particles after calcinations at 350 ^{o}C. The height profile of GO is around 0.8 nm which is reported in the literature [2]. The AFM image of G-TiO$_2$-600 shows the thickness of the oxide film to be ~1 nm.
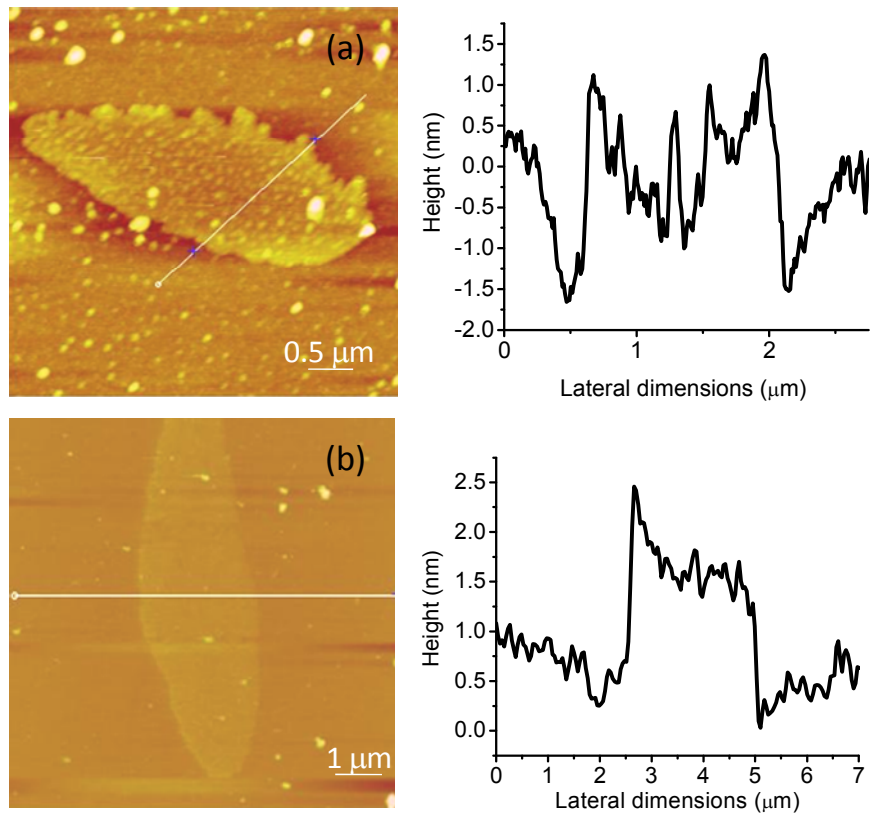

Figure 9. *AFM images of (a) of graphene-TiO$_2$ composite after calcination at 350°C and (b) of TiO$_2$ nanosheets after the removal of graphene at 600 °C. Corresponding Height profiles are given.*

TiO$_2$ is a well known dielectric material [8] with the bulk sample having dielectric constant of 20-30. The TiO$_2$ nanosheets obtained by us has a much higher dielectric constant is shown in Figure 10.
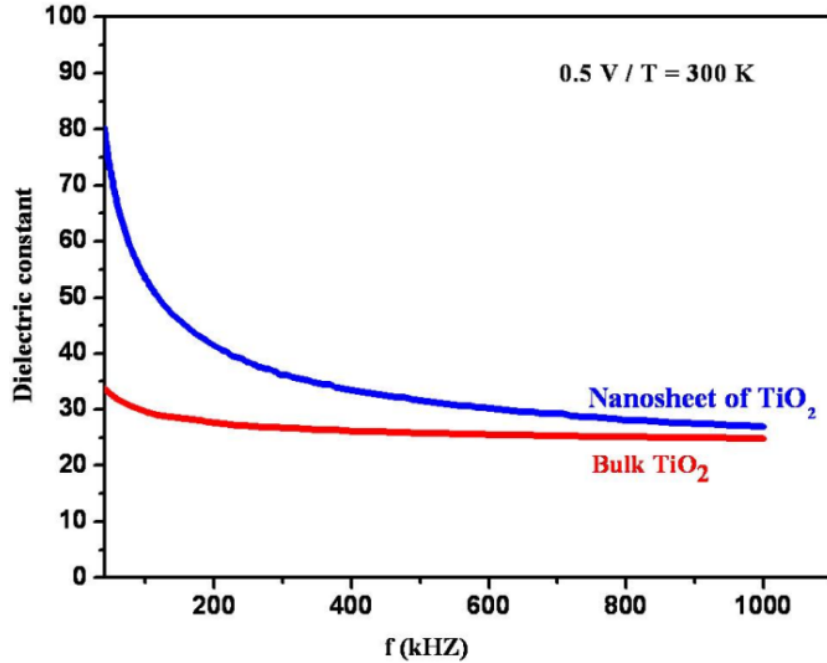
Figure 10. *Frequency-dependent dielectric constant of TiO$_2$ nanosheets compared to bulk TiO$_2$.*

Encouraged by the synthesis of TiO$_2$-bonded graphene, we prepared films of graphene bonded to SiO$_2$ by using SiCl$_4$ as the reagent. In Figure 11(a), we show a SEM image of SiO$_2$-bonded to graphene prepared after 10 cycles of coating and calcined at 350 °C. Figure 11b shows TEM image of sample calcined at 600 ^{o}C.
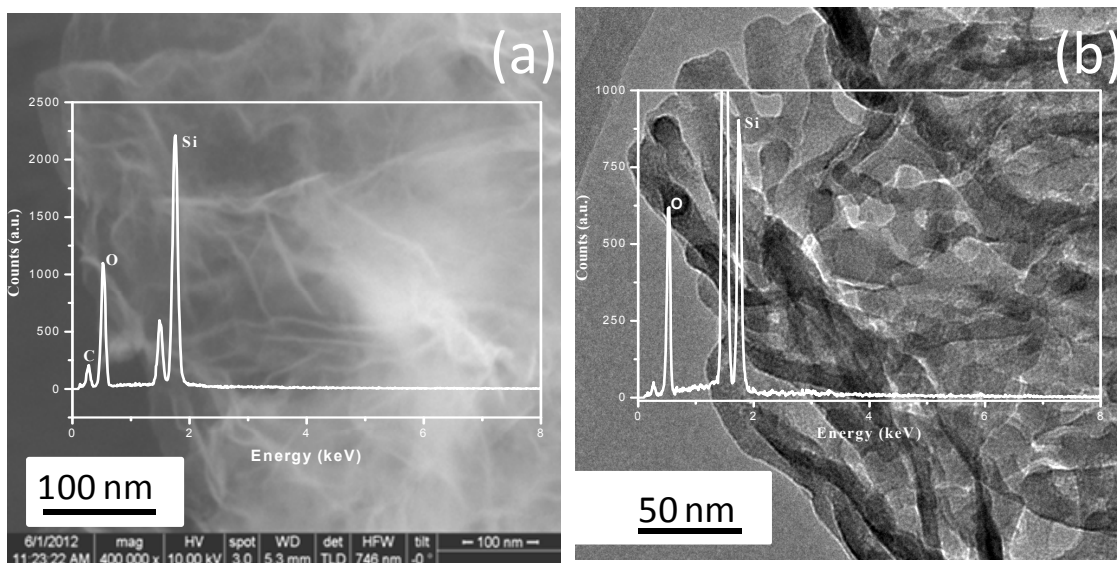
Figure 11. (*a*) *FESEM image of SiO₂-bonded graphene calcined at 350 ℃ and (b) TEM image of SiO₂ nanosheets obtained after calcination of SiO₂-bonded graphene at 600 ℃. Insets show EDX patterns.*

The EDX pattern shows presence of carbon, silicon and oxygen (see inset of Figure 11a). A TEM image of SiO$_2$ nanosheets obtained after calcination of SiO$_2$-bonded graphene sheets at 600 °C is shown in Figure 11b. EDX pattern in Figure 11b shows the presence of only silicon and oxygen (see inset of Figure 11b). The Raman spectra of SiO$_2$ coated samples shows peaks corresponds to graphene both at room temperature and calcination at 350 °C.

The AFM image of SiO$_2$-bonded graphene heated to 350 °C gives a ~5-6 nm thick film. The SiO$_2$ nanosheets were amorphous and SiO$_2$ sheets obtained by calcination at 600 °C were ~2 nm thick, which is shown in Figure 12. EDX pattern of EG-SiO$_2$-600 shows peaks corresponds to only Si and O.
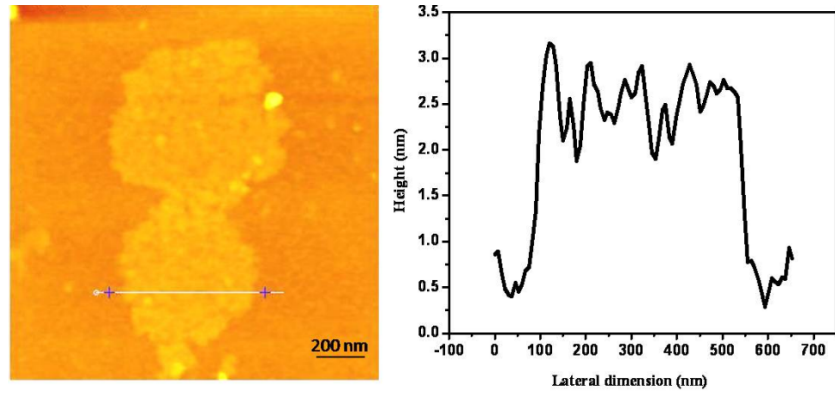
Figure 12. *AFM Image of SiO_2 nanosheets obtained after calcination of SiO_2-bonded graphene at 600 ℃. Height profile is shown.*

We have also been able to bond Al_2O_3 to graphene by using $AlCl_3$ as the reactant. The oxide film shows peaks corresponding to corundum structure of Al_2O_3 after calcination at 600 °C.

Figure 13. *(a) SEM image of Al_2O_3- graphene calcined at 350 ℃ [(c) shows EDAX pattern] and (b) SEM image after calcination of Al_2O_3 -bonded graphene at 600 ℃ [(d) shows Raman spectrum].*

In Figure 13a and b we show the SEM images of Al_2O_3 bonded to graphene calcined at 300 ^{o}C and 600 ^{o}C respectively. Figure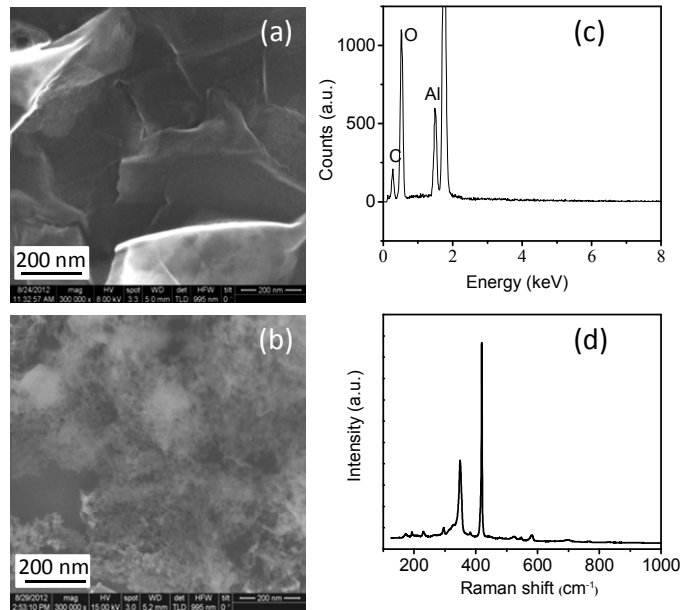 13c corresponds to the EDX pattern of the composite calcined at 350 ^{o}C shows the presence of C, Al and O. Figure 13d shows the Raman spectra of the composite calcined at 600 ^{o}C.

2.1.4 Conclusions

We have developed a new versatile method for obtaining chemically-bonded ceramic oxide coating on graphene to obtain thin films of metal oxides. We speculated that the methodology described here can be used for controlled layer by layer coatings of various metal oxides over graphene. The method described here can also be used for the electrical insulation of graphene in nanocircuits and potential synthesis of ceramic composites with higher toughness.

2.2 Chemically bonded graphene-magnetite composite

Summary*

In this chapter, we describe the synthesis of covalent composite of graphene with Fe$_3$O$_4$. This method involves reacting graphene functionalized with acid chloride groups with amine-containing Fe$_3$O$_4$, resulting in the formation of the amide bond. The composites show enhanced dispersibility in organic solvents like THF, DMF, NMP. Dispersions obtained were stable for several days. Composites show satisfactory magnetization values.

2.2.1 Introduction

Fe$_3$O$_4$ nanocrystals have wide variety of applications in drug delivery and targeting, magnetic resonance imaging, supercapacitor and lithium ion batteries [15]. Superparamagnetic nature of Fe$_3$O$_4$ nanocrystals is a key factor for their broad application in many fields due to their rapid response to the applied magnetic field [16]. It is still challenging to achieve superparamagnetic performance of magnetite nanocrystals when their size is bigger in the composite. Recently hybrid materials of graphene-Fe$_3$O$_4$ have been used as energy storage material and drug delivery applications [17]. However there exist practical problems with these hybrid materials; (i) magnetite particle distribution on the graphene sheets is not even, (ii) Because of the agglomeration of the magnetite nanoparticle, they precipitate from the aqueous solution [18]. To produce water dispersible graphene-Fe$_3$O$_4$,

polymer additives were used, they are practically undesirable [19]. In this regard we are motivated to synthesize graphene-Fe_3O_4 composites of enhanced dispersbility in organic solvents.

2.2.2 Experimental methods

To prepare graphene chemically bonded to Fe_3O_4, the nanoparticles of Fe_3O_4 were prepared by the method reported in the literature [17]. In a typical synthesis, 6.5 g of 1, 6-hexadiamine, 2.0 g of sodium acetate and 1.0 g of $FeCl_3$ were vigorously stirred in 30 ml of ethylene glycol at 50 °C until a clear yellow solution was obtained. The resultant solution was transferred into a Teflon-lined stainless-steel autoclave and kept at a temperature of 200 °C for 6 h. The amine-coated Fe_3O_4 nanoparticles so obtained were reacted with graphene containing acid chloride groups (G-COCl). G-COCl was prepared by refluxing graphene oxide with excess of thionyl chloride for 12 h, the excess thionyl chloride being removed under vacuum. In a typical reaction, 20 mg of the amine-coated Fe_3O_4 was dispersed in 10 ml dry DMF and sonicated for 10 min. The suspension was added to G-COCl, sonicated for 10 min and refluxed at 70 °C for 12 h under nitrogen. The resultant solution was centrifuged, and the solid product washed with water, ethanol and dried in vacuum.

2.2.3 Results and discussion

Fe_3O_4 magnetite nanoparticles are attached to graphene through amide bond. The IR bands (Figure 1) observed at around 588 cm^{-1} can be ascribed to Fe-O vibrational mode of Fe_3O_4. The IR bands at 1595 cm^{-1} attributed to the free amine group such as NH_2 scissoring. The peak at 1723 cm^{-1} corresponded to C=O group in carboxylic acid and carbonyl moieties.

after amidation reaction, C=O stretching shifted to 1690 cm^{-1} implies that Fe_3O_4 NPs were linked to GO surface by covalent bonding which is shown in IR spectrum Figure 1 (red curve). 2941 and 2857 cm^{-1} peaks corresponds to CH_2 stretching [18].
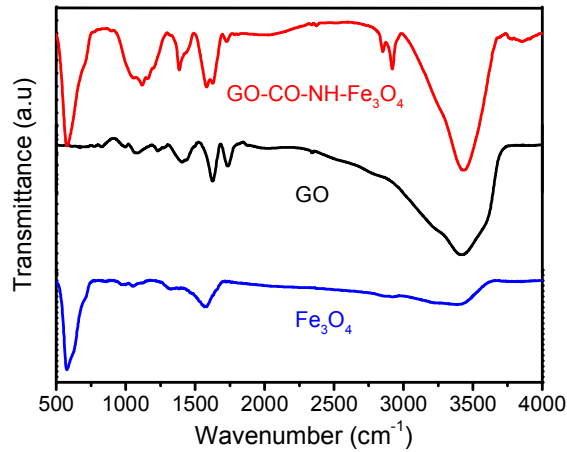

Figure 1. *IR spectra of Fe_3O_4, GO and GO-CO-NH-Fe_3O_4.*

The IR spectrum (Figure 1 red curve) clearly shows the presence of the amide carbonyl stretching band in the graphene-Fe_3O_4 composite. The morphology of GO-Fe_3O_4 composite particles is shown by the TEM images in Figure 2. Dense Fe_3O_4 particles are found at the edge of the sheets, since graphene oxide has most carboxyl functional groups at the edges. The particle size of Fe_3O_4 is in the range of 10-15 nm
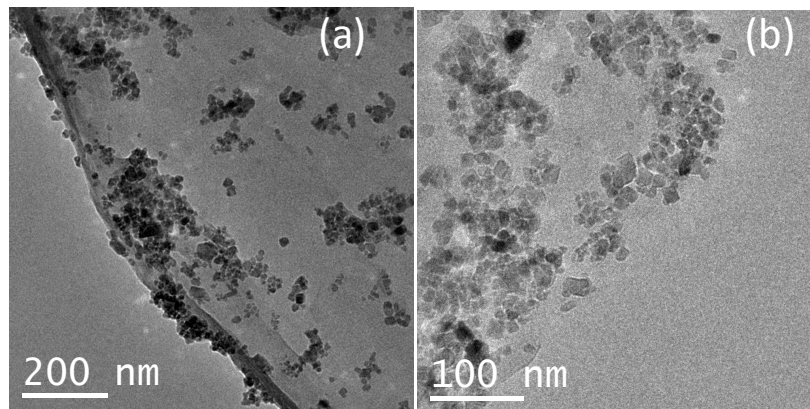
Figure 2. *TEM images of the GO-Fe_3O_4 composite.*

Figure 3. *Dispersions of the GO-Fe$_3$O$_4$ composite in different solvents.*

In Figure 4, we show M-H curves of the GO-Fe$_3$O$_4$ composite. The saturation magnetization (M_s) of GO-Fe$_3$O$_4$ is 43.18 emu/g which is smaller than the M_s value of amine functionalized Fe$_3$O$_4$ (84.28 emu/g) [19, 20].
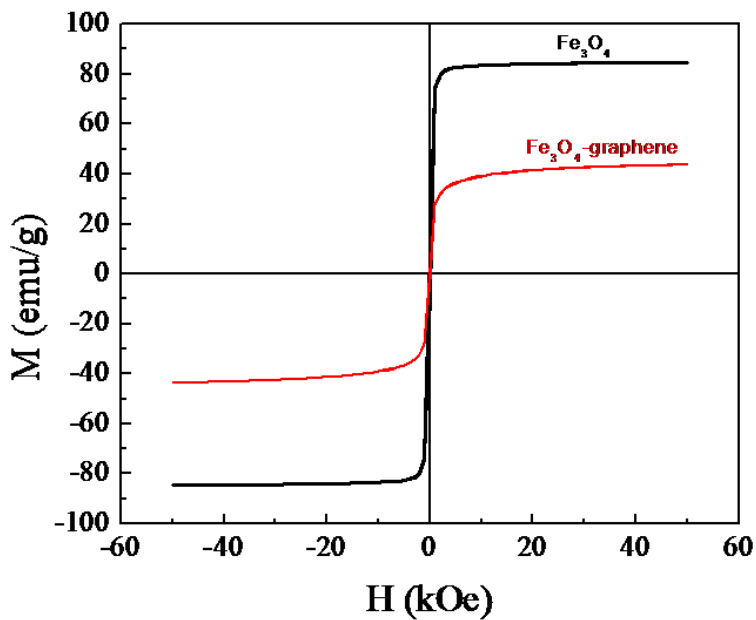
Figure 4. *M-H curve of amine-functionalised Fe$_3$O$_4$ and the GO-Fe$_3$O$_4$ Composite.*

2.2.4 Conclusions

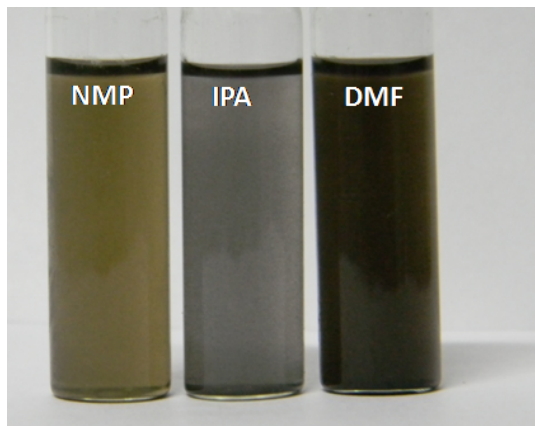We have been able to chemically bond Fe_3O_4 nanoparticles to the graphene surface through amide bonding. The magnetite nanoparticles found to be immobilized on the surface of graphene even after long sonication. Stable dispersions of graphene-Fe_3O_4 composites were obtained in different solvents like NMP and DMF. Fe_3O_4 nanoparticles chemically bonded to graphene exhibit satisfactory magnetization values for use in diagnostics and other applications.

2.3 References

[1]   A. K. Geim, K. S. Novoselov, Nat. Mater. 6 (2007) 183.

[2]   K. S. Novoselov, A. K. Geim, S. V. Morozov, D. Jiang, Y. Zhang, S. V. Dubonos, I. V. Grigorieva, A. A. Firsov, Science. 306 (2004) 666.

[3]   C. N. R. Rao, A. K. Sood, (ed), Graphene, Wiley-VCH Weinheim, 2013.

[4]   C. N. R. Rao, A. K. Sood, K. S. Subrahmanyam and A. Govindaraj, Angew. Chem. Int. Ed. 48 (2009) 7752.

[5]   H. S. S. R. Matte, A. Gomathi, A. K. Manna, D. J. Late, R. Datta, S. K. Pati, C. N. R. Rao, Angew. Chem. Int. Ed. 49 (2010) 4059.

[6]   K. S. Novoselov, D. Jiang, F. Schedin, T. J. Booth, V. V. Khotkevich, S. V. Morozov, A. K. Geim, Proc. Natl. Acad. Sci. U.S.A. 102 (2005) 10451.

[7]   J. N. Coleman, M. Lotya, A. O'Neill, S. D. Bergin, P. J. King, U. Khan, K. Young, A. Gaucher, S. De, R. J. Smith, I. V. Shvets, S. K. Arora , G. Stanton, H. Kim, K. Lee, G. T. Kim, G. S. Duesberg, T. Hallam, J. J. Boland, J. J. Wang, J. F. Donegan, J. C. Grunlan, G. Moriarty, A. Shmeliov, R. J. Nicholls, J. M. Perkins, E. M. Grieveson, K. Theuwissen, D. W. McComb, P. D. Nellist and V. Nicolosi, Science. 331 (2011) 568.

[8]   X. Wang, S. M. Tabakman, H. Dai, J. Am. Chem. Soc. 130 (2008) 8152.

[9]   H. Cao, B. Li, J. Zhang, F. Lian, X. Kong, M. Qu, J. Mater. Chem. 22 (2012) 9759.

[10] H. Zhang, X. Lv, Y. Li, Y. Wang, J. Li, ACS Nano. 2010 (4) 380.

[11] M. Miyauchi, A. Nakajima, T. Watanabe, K. Hashimoto, Chem. Mater. 2002 (14) 2812.

[12]   T. Kamegawa, N. Suzuki, H. Yamashita Energy Environ. Sci. 2011 (4) 1411.

[13]   W. S. Hummers, R. E. Offeman, J. Am. Chem. Soc. 80 (1958) 1339

[14]   A. Gomathi, S.R.C. Vivekchand, A. Govindaraj, C. N. R. Rao, Adv. Mater. 17 (2005) 2757.

[15]   B. Li, H. Cao, J. Shao, M. Qu, J. H. Warner, Chem. Commun. 47 (2011) 10734.

[16]   X. Li, X. Huang, D. Liu, X. Wang, S. Song, L. Zhou, H. Zhang, J. Phys. Chem. C. 115 (2011) 21567

[17]   F. Zhang, J. Jin, X. Zhong, S. Li, J. Niu, R. Li, J. Ma, Green Chem. 13 (2011)   1238.

[18]   W. Hu, L. Li, W. Tong , G. Li, Chem. Commun. 46 (2010) 3113.

[19]   B. Li, H. Cao, J. Shao, M. Qu, J. H. Warner, J. Mater. Chem. 21 (2011) 5069.

[20]   B. Das, B. Choudhury, A. Gomathi, A. K. Manna, S. K. Pati, C. N. R. Rao, Chem. Phys. Chem. 2011 (12) 937.

CHAPTER 3

COMPOSITES OF INORGANIC GRAPHENE ANALOGUES

3.1 Synthesis, characterization and electrical properties nanocomposites of molybdenum disulphide with PANI

Summary*

Composites of polyaniline (PANI) have been prepared with few-layer molybdenum disulphide (MoS_2) by *in -situ* polymerization of PANI in the presence of MoS_2. X-ray diffraction, Electron microscopy, UV-Vis and Raman spectroscopy have been used for the characterization of PANI-MoS_2 composites. Changes in UV-Vis and Raman spectra show considerable interaction between few-layer MoS_2 and PANI. Electrical resistivity of the composites have been measured by four probe technique and compared with those of the MoS_2 and PANI. Composite shows electrical resistivity in between few-layer MoS_2 and PANI.

3.1.1 Introduction

Composites of polymers with nanomaterials are of scientific and industrial importance because of the enhanced mechanical and electrical properties of polymer with nanofiller [1 , 2]. Ajayan *et al*. [3] first reported the synthesis of carbon nanotube-polymer composites by *ex-situ* polymerization. After that there have been considerable efforts to prepare composite functional materials of polymer-carbon nanotube composites with desirable electrical and mechanical properties [4]. Polyaniline (PANI) and polypyrrole (PPy) are conductive polymers incorporated in carbon nanotube matrix; these composites have potential applications in photovoltaic devices [5]. PANI and PPy polymers have been chosen to make composites because of their environmental stability, low cost and easy procesasbility. PANI composite films with high current density and novel surface characteristics have been obtained by Downs *et al. [6a]* by the polymerization of aniline monomer on multi-walled carbon nanotube (MWNTs) electrodes. Even at lower concentrations, MWNTs enable percolation into the PANI network because of their high aspect ratio. These composites have potential applications as printable conductors for electronic device [7].

Cochet *et al*. [8] prepared composites of PANI-MWNTs by *in-situ* polymerization whose electrical resistivity is lower than that of pure PANI. Zengin *et al*. [9] prepared composites of PANI with MWNTs by *in-situ* as well as *ex-situ* polymerization methods. These composites have shown electrical conductivity in between MWNTs and pure PANI. Strong coupling between CNTs and polyaniline in indicated by change in sign of the

magnetoresistance at lower temperature [10]. Rao and coworkers made the composites of PANI with Zinc Oxide (ZnO NW) and Ruthenium Oxide (RuO$_2$ NW) nanowires of various compositions by *in-situ* polymerization. Where ZnO is a wide band gap semiconductor with a band gap of 3.37 eV where as RuO$_2$ is metallic. These composites show room temperature resistivity varying between 0.01-400 Ω cm depending on the composition of nanowires [11]. Composites formed by *in-situ* polymerisation were found to show better interactions than the *ex-situ* methods [9].

On the other hand conventional polymer matrix made by bulk materials often require large amount of filler (~ 60 wt %) in order to achieve desired properties. In contrast marked reinforcement in the property of polymer can be obtained by using relatively small amount of nanofiller (~ 2 wt %) [6b]. Rao and coworkers incorporated few-layer functionalized graphene (FG) into polyvinyl alcohol and poly(methyl methacrylate) matrix. Relatively small (~ 0.6 wt %) amount of FG incorporation into polymer, shown enhancement in both elastic modulus and hardness [6b]. Filler material is functionalized in order to increase interaction between the polymer and filler material in matrix.

Few-layer MoS$_2$ is an inorganic analogue of graphene having a direct band-gap of 1.7 eV, with trigonal prismatic structure and has inter-layer spacing of 0.67 nm [12]. Wide range of composite materials of few-layer MoS$_2$ with various polymers like PPy and PANI are reported, where these polymer chains are inserted between the layers of few-layer MoS$_2$. Interlayer spacing of is found to be increased after polymer insertion [13].

PANI known to exist in three different oxidation states, (a) Leucoemeraldine; fully reduced form of PANI, (b) Pernigraniline; is fully oxidised form of PANI and (C) Emeraldine; is half oxidized and half reduced form, which has both amine and imine link. Protonated form of emeraldine called emeraldine salt, which is the electrically conducting form appears green in colour [14].
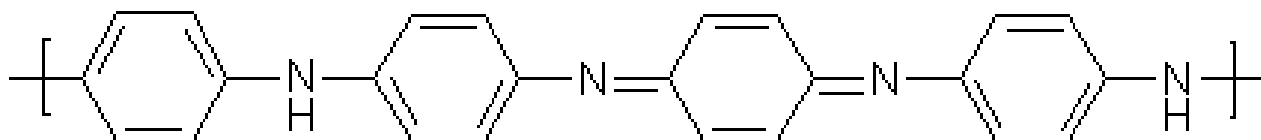
EMERALDINE SALT

We are interested in studying the interaction of PANI with MoS_2. We have characterized PANI-MoS_2 composites by Raman, UV-Vis spectroscopy and measured electrical resistivity of various compositions by four probe method.

3.1.2 Experimental details

Few-layer MoS_2 is prepared by the reaction of molybdic acid with thiourea at 600 ^{o}C in argon atmosphere for 6 hr [15]. HCl doped PANI was prepared by the method similar to that of Fite *et al*. [7]. In a typical synthesis, ammoniun persulfate (5.6 g) was dissolved in 100 ml of 1 m aqueous HCl solution and was cooled to 0 ^{o}C. This oxidizing agent was slowly added to the aniline solution under sonication at 0 ^{o}C. The sonication was carried out for

another 2 h after the addition of oxidizing agent. The product was filtered, washed thoroughly with distilled water and later with methanol to remove oligomers [16,17].

We have prepared composites of few-layer MoS_2 with PANI by in-situ polymerization method. In a typical synthesis of PANI-MoS_2 (20 wt % of MoS_2) composite, an ammonium persulfate (0.6867g dissolved in 13.7 ml of 1 M aqueous HCl solution) was slowly added to a mixture of aniline (0.67 g) and few-layer MoS_2 (0.13 g) which is taken in a round bottomed flask containing 13.7 ml of 1 M HCl under sonication at 0 ^{o}C. Sonication was continued for two more hours. The product was washed with water (to remove unreacted HCl and ammonium persulfate) and then with methanol (to remove the oligomers). The filtered sample was dried in vacuum at room temperature for 24 h to ensure the absence of moisture, which affects the conductivity of PANI [18]. The two PANI-MoS_2 composites prepared by us are: 20 and 30 wt % of few-layer MoS_2-PANI.

The composites and the parent few-layer MoS_2 were characterized by X-ray powder diffraction (XRD), Scanning electron microscopy (SEM), Transmission electron microscopy (TEM), Infrared spectroscopy and Raman spectroscopy. The electric properties were measured by the 4-probe technique between 30 ^{o}C and -258 ^{o}C. FTIR Spectra were recorded with KBr pellet using Bruker Tensor 27 IR spectrometer. Scanning electron microscope (SEM) images were recorded with a FEI NOVA NANOSEM 600. Transmission electron microscope (TEM) images were viewed with a JEOL TEM 3010 instrument fitted with a

a Gatan CCD camera operating at an accelerating voltage of 300 kV. For TEM, samples were prepared by dispersing the product in ethanol. A drop of the suspension was then put it on a holey carbon grid and allowed the solvent to evaporate. Raman spectra were recorded at different locations of the sample using Jobin Yvon LabRam HR with 514 nm Ar laser.

3.1.3 Results and Discussion

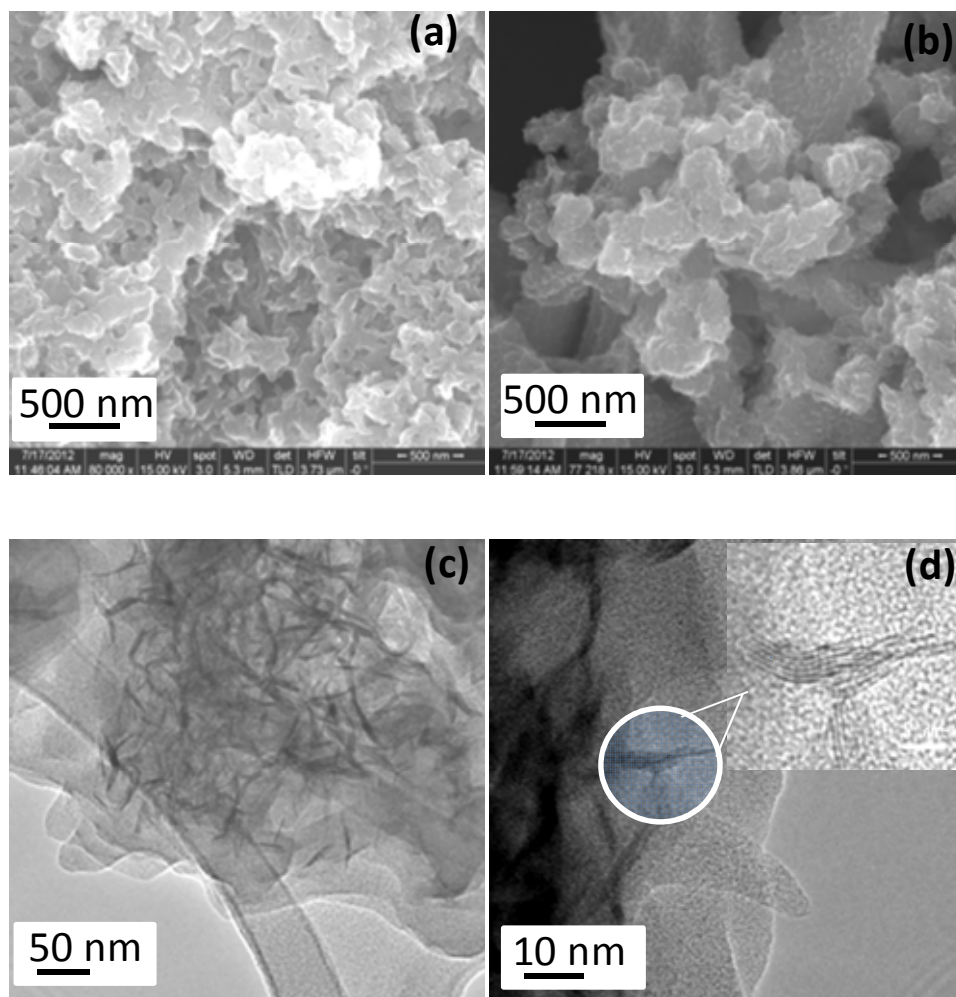In Figure 1, we show the SEM and TEM images of PANI-MoS$_2$ composites.

Figure 1. *SEM images of a) PANI and (b) PANI-MoS$_2$ composites. (C) and (D) TEM images of PANI-MoS$_2$ composites. (Inset HRTEM image).*

Electron Microscopy images in Figure 1, confirms the formation of homogeneous composite. Few-layer MoS_2 has negative charges due to dangling sulphur bonds, where as polyaniline growth takes place on by columbic adsorption of positively charged aniline monomer over few-layer MoS_2 by *in-situ* polymerization. This was confirmed in TEM images (Figure 1d), where we observed growth of polyaniline over few-layer MoS_2. Inset in Figure 1d shows few-layer MoS_2 which is composed of 6-7 layers embedded in polyaniline matrix during *in-situ* polymerization.

In Figure 2 we show UV-Vis spectra of PANI-MoS_2 composites. The spectra show all the typical bands of polyaniline. Peak at 340 nm corresponding to π-$\pi*$, where as 440 nm corresponding to polaron-$\pi*$ transition [19].
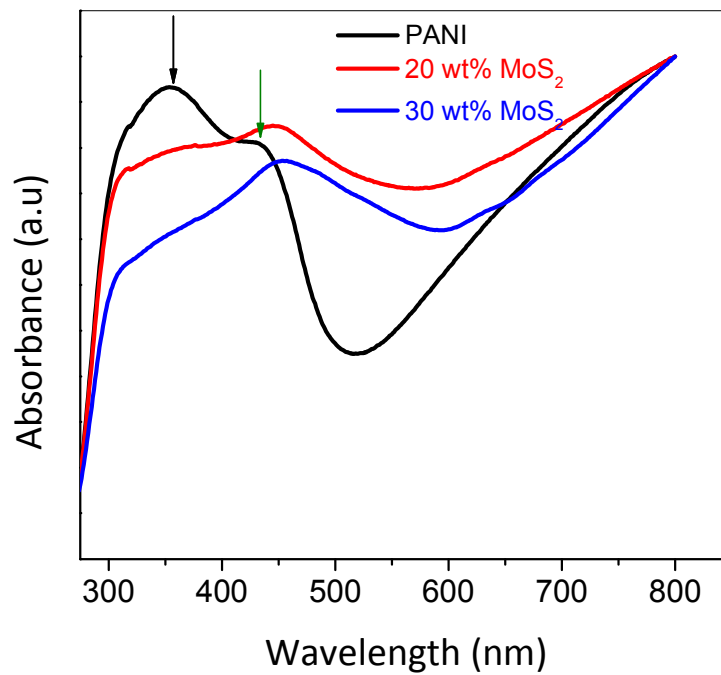

Figure 2. *UV-Vis absorption spectra of PANI and composites of PANI-MoS₂.*

The polaronic band is red-shifted with the increase in composition of MoS_2. This red-shift is typical of conducting polymer and is due to increase in delocalization of polarons resulting from the increase in the amount of MoS_2 in the nanocomposites. UV-Vis spectra reveal that the few-layer MoS_2 is quite well interacting with the PANI which results in the stabilization of polaronic structure [18].

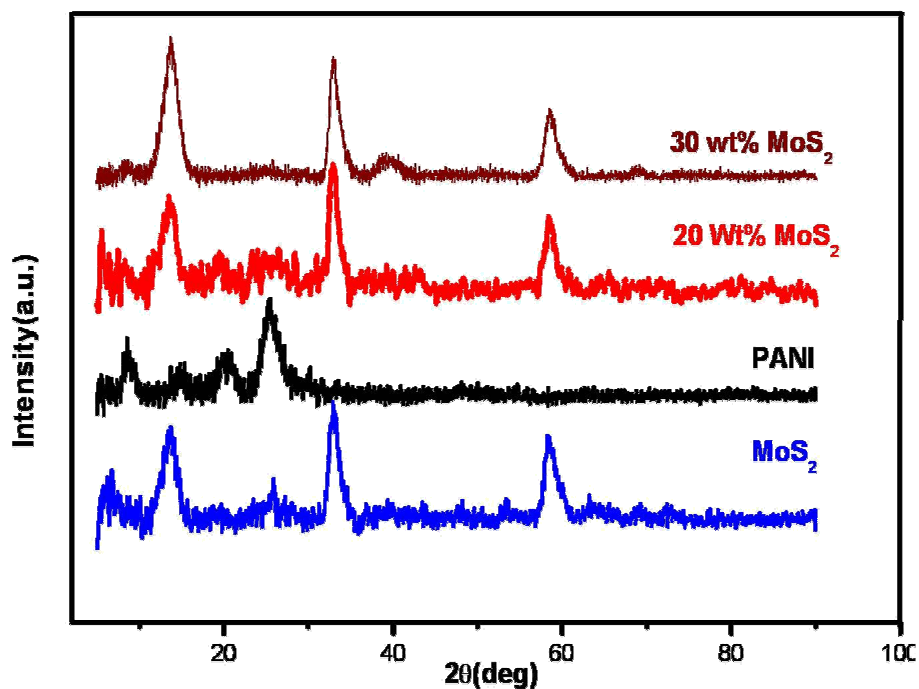In Figure 3, we show the XRD pattern of PANI, few-layer MoS_2 and PANI-MoS_2 composites.

Figure 3. *XRD pattern of MoS$_2$, PANI and PANI-MoS$_2$ Composites.*

For PANI, emeraldine state characteristic peaks were observed at 2θ value of 15.3^o, 20.4^o and 26.28^o corresponding to the crystal planes of (011), (020) and (200) respectively [21]. Few-layer MoS$_2$ shows peaks at 2θ value of 33° and 69.8^o, which corresponds to (100) and (201) crystal planes. In composites, few-layer MoS$_2$ peaks are dominated because of high crystalline nature.
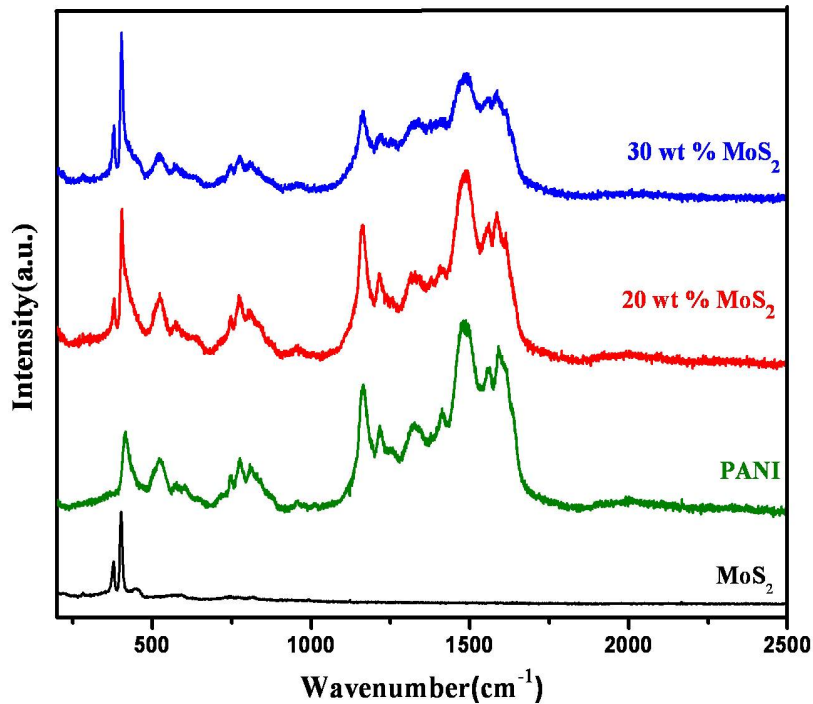

Figure 4. *Raman spectra of MoS$_2$, PANI and PANI-MoS$_2$ Composites.* ..

The Raman spectra (Figure 4) of few-layer MoS$_2$ display two bands at 380 and 430 cm^{-1}, which corresponding to A$_{1g}$ and E$_{2g}$ phonon vibration modes. PANI gives bands at 1590, 1560, 1323, 1215 and 1160 cm^{-1}, corresponding to benzenoid C-C stretching, quinoid C=N stretching, C-N$^{+.}$ stretching, C-H bending of quinoid and benzenoid respectively. Indicates the formation of emeraldine salt [22-24]. In composite, there is an increase in

relative intensity of C-H bending of benzenoid compared to quinoid band, this confirms the stabilization of polaronic structure [25]. PANI-MoS$_2$ composites show peaks corresponds to both MoS$_2$ and PANI. The Peak intensity of MoS$_2$ is increased with increase in wt % of MoS$_2$ in the composite.
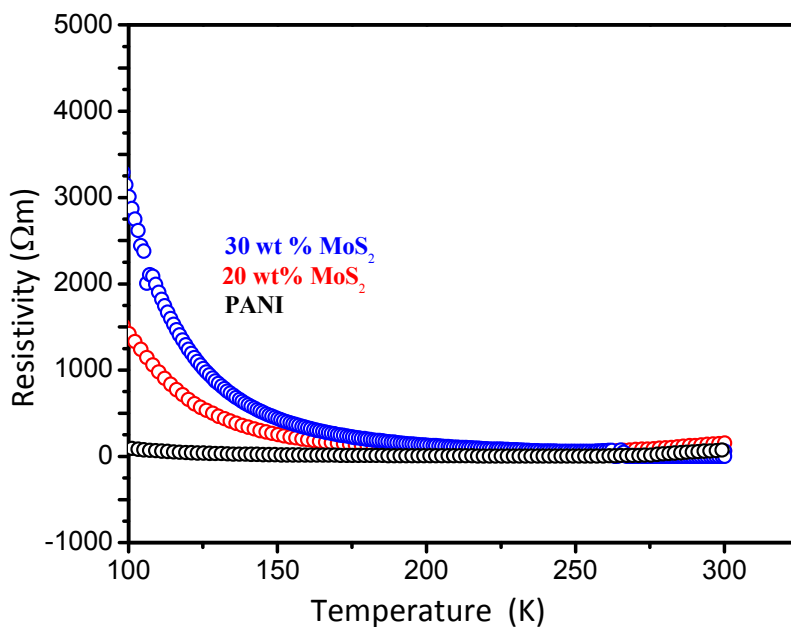

Figure 5. *Resistivity vs. temperature plots for PANI-MoS$_2$ composites.*

The electrical conductivity in conducting polymer arises due to the introduction of charge carriers by doping. The doped form will exhibit more conductivity than pure polymer. By looking at variable temperature electrical transport properties of the composites (Figure 5), we can conclude that PANI-MoS$_2$ composites show strong temperature dependence at lower temperature rather than at room temperature, there is not much difference in the resistivity of parent PANI and its composites. This can be explained by considering the factor that at room temperature, the contribution by MoS$_2$ for resistivity is negligible. Also we can

see from the Figure 5, that pure PANI shows a very weak temperature dependence of resistivity [26].

3.1.4 Conclusions

Composites of PANI with few-layer MoS_2 can be prepared by *in-situ* polymerization of aniline over MoS_2 using HCl as the dopant. The PANI-MoS_2 composites can be characterized satisfactorily by Raman, UV-Vis spectroscopy and electron microscopy. The changes in Raman and UV-Vis spectra show that there is definite interaction between PANI and few-layer MoS_2. The electrical resistivity of the nanocomposites at lower temperature differs from that of PANI. The present study establishes that electrical resistivity of PANI-MoS_2 composites at lower temperature can be manipulated through the variation of composition.

3.2 Electrical properties of nanocomposite of molybdenum disulphide with graphene

Summary*

Composites of few-layer MoS_2 with reduced graphene oxide (RGO) have been prepared by physical method. It involves mixing the dispersions of MoS_2 and GO by sonication, followed by subsequent reduction with hydrazine hydrate. X-ray diffraction, Electron microscopy and Raman spectroscopy techniques have been used for the characterization of RGO/MoS_2 composites. X-ray diffraction and Raman spectra indicate the presence of both few-layer MoS_2 and RGO in the composites. Electrical resistivity of the composites have been measured by four probe technique and compared with those of the MoS_2 and RGO. RGO/MoS_2 composites show electrical resistivity in between few-layer MoS_2 and RGO.

3.2.1 Introduction

Few-Layer MoS_2 is an inorganic analogue of graphene; a typical layered transition metal disulfide consists of three stacked atom layers where central layer contain molybdenum atom which is sandwiched between sulphur layers. Layers are stacked together by Van der waals forces with an interlayer separation of 0.67 nm [12]. Because of their layered structure they showed excellent electrochemical performance as anode material for lithium ion batteries. Layered structure allows Li ion to intercalate and exfoliate. For MoS_2 1131 mA h g^{-1} is the highest reported value of specific capacity with a current of 50 mA h g^{-1} [28]. Graphene has extraordinary electronic behavior, MoS_2 growth on the surface increases its electrical conductivity and electrochemical performance [28]. MoS_2/graphene composites with photocatalyst TiO_2 results in enhanced hydrogen production and high catalytic activity towards tri iodide reaction in dye sensitized solar cells [30].

Till date, the methods reported in the literature for the synthesis of MoS_2/graphene composites follows hydrothermal technique [31]. Intial precursors such as ammonium molybdate, sodium hydroxide were mixed with graphene oxide and reaction was carried out hydrothermally. But hydrothermal methods suffer from the drawbacks like less lateral dimension of MoS_2 and uncontrolled composition. In this regard we are interested in making composites of MoS_2 with graphene, of different composition by physical method. Few-layer MoS_2 and graphene oxide dispersions were made in water and sonicated for longer durations and GO is reduced to RGO by hydrazine hydrate to regain electrical conductivity.

3.2.2 Experimental details

Few-layer MoS_2 is prepared by the reaction of molybdic acid with thiourea at 600 ^oC in an argon atmosphere for 6 hr [15]. Graphite oxide is prepared by modified hummer's method [32]. To prepare nanocomposites of MoS_2/RGO with 1:1(wt/wt) ratio, 15 mg of graphite oxide is dispersed in 5 ml water and 15 mg few-layer MoS_2 dispersed in 5 ml DMF by sonication. The dispersions were mixed and sonicated together for 30 min. Finally refluxed with hydrazine hydrate (500 µl) for overnight.
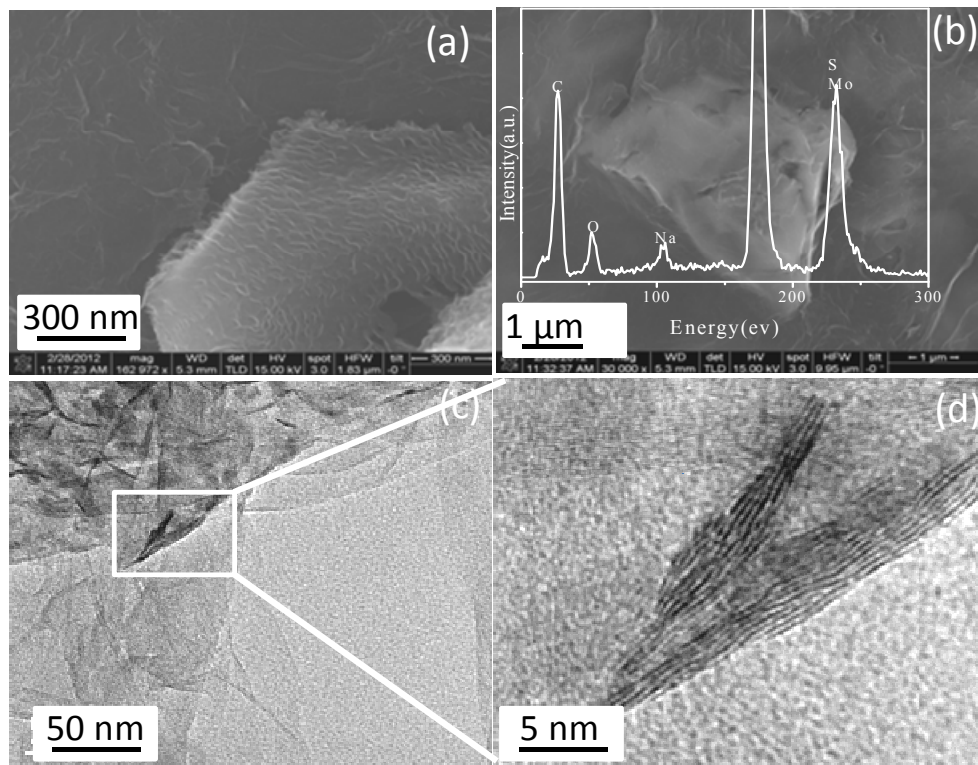
3.2.3 Results and Discussion

Figure 1. (a) *FESEM image (b) EDAX pattern and FESEM image (c) TEM image and (d) high resolution TEM image of 1:1 RGO-MoS$_2$ composite.*

Electron microscopy images confirm the formation of homogeneous composites (Figure 1). EDAX (Figure 1b) pattern indicates that presence of carbon, molybdenum and sulphur in the composites. Figure 1c shows few-layer MoS_2 embedded in between RGO layers. This is confirmed by the HRTEM image (figure 1d). This shows two types of interlayer spacings: 0.35 nm and 0.68 nm, which corresponds to RGO and few-layer MoS_2 respectively.

The XRD pattern (Figure 2) of the composites shows peaks correspond to both RGO and MoS_2. In composites a broad hump at 2θ value of 26° is observed due to RGO [33] along with the peaks of MoS_2. Raman spectra shows that, the increase in proportion of MoS_2, results in the enhancement of graphene D-band intensity at 1350 cm^{-1}.While that of the G-band remains constant. I_D/I_G ratio shows only a slight increase with increase in proportion of MoS_2 in the composite. We have not observed any significant shift in the G-band (1591 cm^{-1}) of graphene in composites [34].
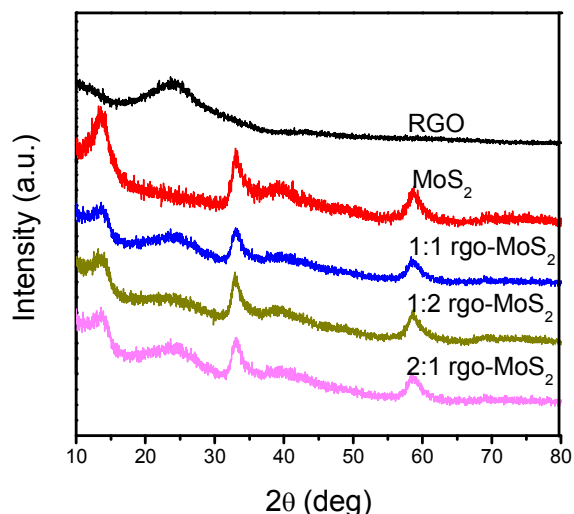

Figure 2. *XRD pattern of RGO, MoS₂ and RGO-MoS₂ composites.*

Electrical resistivity measurements (Figure 5) show that the resistivity of the nanocomposite increases with lowering temperature and follows a trend similar to that of RGO. With the increasing proportion of RGO in the composite, the resistivity decreases progressively.
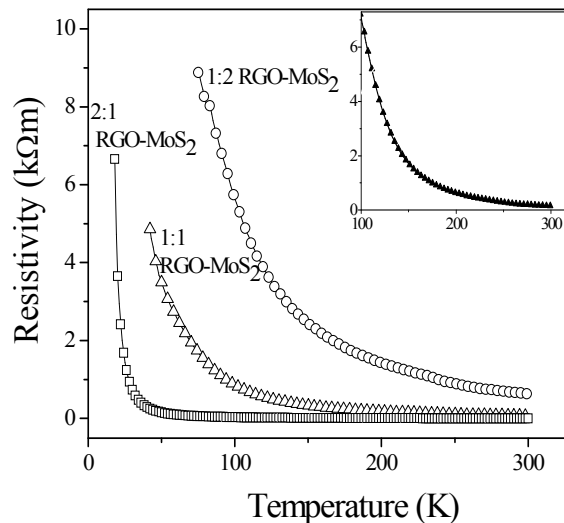

Figure 5. *Resistivity vs temperature plots for RGO/MoS₂ composites. Inset show RGO resistivity curve.*

3.2.4 Conclusions

Composites of RGO with various proportion of few-layer MoS_2 have been prepared by physical method. The RGO/MoS_2 composites have been characterized satisfactorily by Electron microscopy, XRD and Raman, spectroscopy. XRD and Raman spectra show the peaks correspond to both RGO and few-layer MoS_2. The electrical resistivity of the nanocomposites shows semiconducting behavior. The present study establishes that electrical resistivity of RGO can be manipulated by the variation of composition of few-layer MoS_2 in the composites.

3.3 Graphene-Few-layer boron nitride composites

Summary*

Few-layer BN is an insulator. Its electrical conductivity can be enhanced by incorporating into conducting matrix like graphene. Randomly stacked BN and graphene composites have been obtained by mixing dispersions of the two in suitable solvents. We have also prepared the covalent composites of BN with graphene using amine groups on the BN surface. BN attach covalently to graphene, through the carbonyl chloride functional groups. Composites were characterized by electron microscopy and Raman spectroscopy.

3.3.1 Introduction

The new forms of carbon have aroused great interest in recent years. Besides the zero-dimensional fullerenes and one dimensional nanotubes, two-dimensional graphene [35, 36] has open up new directions of research with regard to the properties of low-dimensional materials. Hexagonal boron nitride (h-BN) which has a structure similar to that of graphite can exist in the form of nanotubes. Recently, single-layer and few-layer graphene-like structure of BN have been prepared and characterized [37]. BN is an insulator while graphene is a gap-less conductor. Graphene also exhibits other novel properties such has high surface area and has been doped with boron and nitrogen. Hexagonal boron nitride has a wide band gap of 5.5 eV. High Band gap and and poor solubility are the bottlenecks associated with BN. Goldberg *et al.* [38] reported the composites of BN formed by covalent functionalization of BNNTs (boron nitride nanotubes) with long chain alkyl chlorides (steroyl chloride). Covalent composites shows reduced band gap and enhanced solubility in organic solvents. Composites of boron nitride with π-conjugated polymers were reported; here BN interacts with polymer through π- π interaction [39]. In this regard we synthesized RGO/BN composites by both covalent and non covalent functionalization.

3.3.2 Experiemental Section

h-BN is prepared by the reaction of Boric acid with urea (1:48) in nitrogen atmosphere. Exfoliated graphene (EG) chemically bonded to BN (1:2 wt/wt) has been prepared by using the amino group on the BN surface (BN-NH$_2$) and the carboxyl groups on the oxidized surface of graphene (COOH-EG). In the first step, conc. nitric acid (2 ml), conc.

sulfuric acid (2 ml) and water (16 ml) was added to EG and subsequently heated in microwave oven for 10 minutes. Further, the sample was heated at 100 $^{\circ}$C for 12 hours under hydrothermal conditions. The product was washed with distilled water and centrifuged repeatedly to remove traces of the acid. The so yielded graphene was functionalized with –OH and –COOH groups. The acid treated EG was refluxed with excess $SOCl_2$ for 12 hours and the unreacted $SOCl_2$ was removed under vaccum. 5 mg of BN and 2 mg EG-COOH dispersed in 5 ml DMF (di-methyl formamide) by sonication. Subsequently 5 mg EDC (1-Ethyl-3-(3-dimethylaminopropyl)carbodimide and 2 mg DMAP (4-Dimethylaminopyridine) were added. Here EDC is the coupling agent and DMAP acts as catalyst. The mixture was heated to reflux at 80 $^{\circ}$C overnight.

Physical mixture of BN and graphene has been prepared by the reaction of graphite oxide (GO) and BN. GO prepared by modified hummers method. To prepare nanocomposites of BN/RGO with 1:1(wt/wt) ratio, 15 mg of graphite oxide is dispersed in 5 ml water and 15 mg of few-layer BN dispersed in 5 ml DMF by sonication. The dispersions were mixed and sonicated together for another 30 min. Finally refluxed with hydrazine hydrate (500 µl) for overnight. We have characterized BN/RGO composites by Raman, XRD and electron microscopy.

3.3.3 Results and discussion

In Figure 1a we show a representative SEM image of the BN/RGO composites prepared by the second procedure. Figure 1 shows BN sheets embedded in graphene matrix. TEM images and EDAX of the composite prepared by both physical and covalent functionalization is shown in inset Figure 1b and 1c respectively.
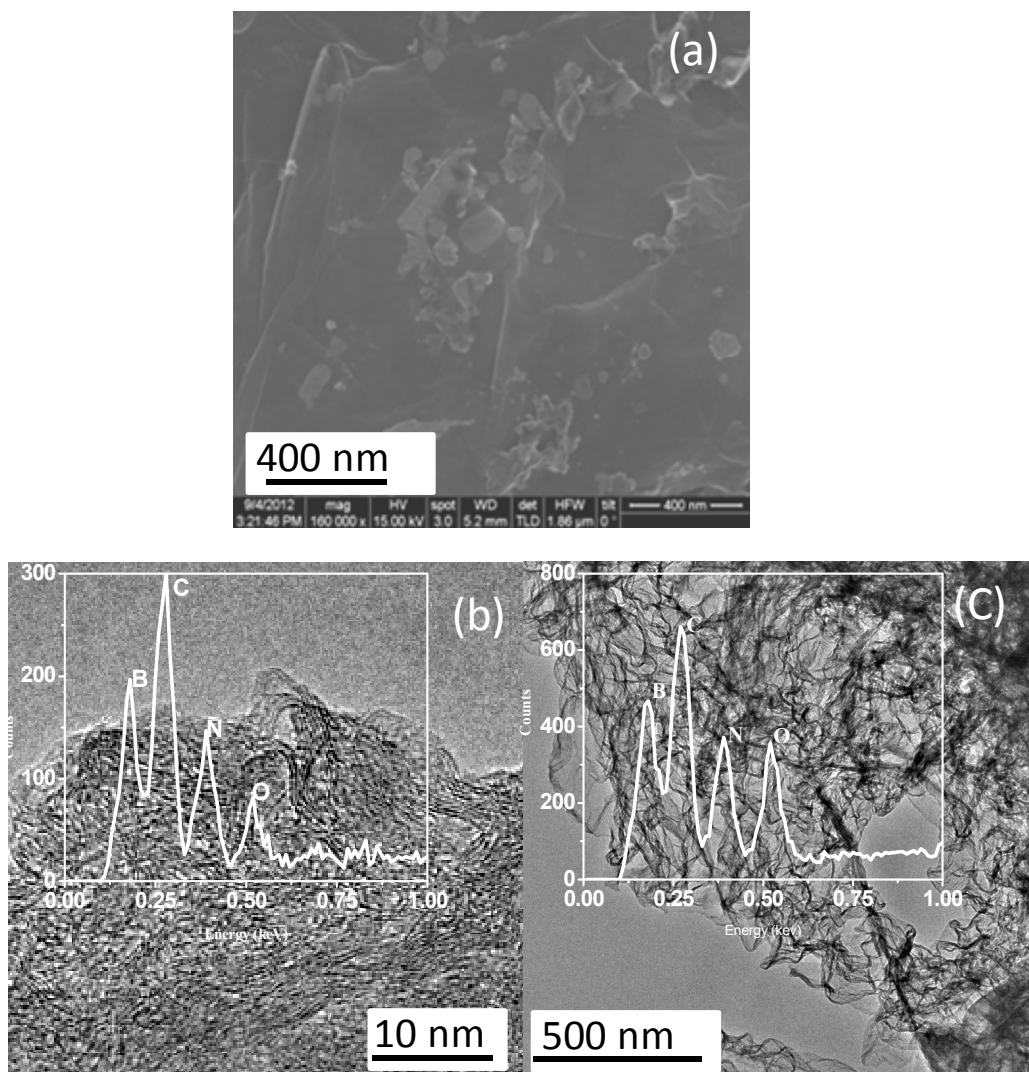

Figure 1. *(a) SEM image of BN/RGO physical mixture, TEM image and the corresponding EDAX spectra of (b) a physical mixture of BN/RGO and (c) covalently attached BN and Graphene*

76

Random stacking of BN and graphene can be accomplished by mixing solutions or dispersions of the two in suitable solvents. Such composites would contain graphene and BN sheets and exhibit additive Raman spectra. In figure 2 shows the Raman spectrum of such composite, exhibiting the band BN band appearing next to the D-band of graphene. The Raman spectra of the composites show D-band at 1340 cm^{-1} and G-band at 1600 cm^{-1}. After peak fitting we can resolve the peak at 1340 cm^{-1} into 1340 cm^{-1} and 1370 cm^{-1}. Raman band centered at 1370 cm^{-1} can be assigned to the E$_{2g}$ tangential mode of the h-BN.
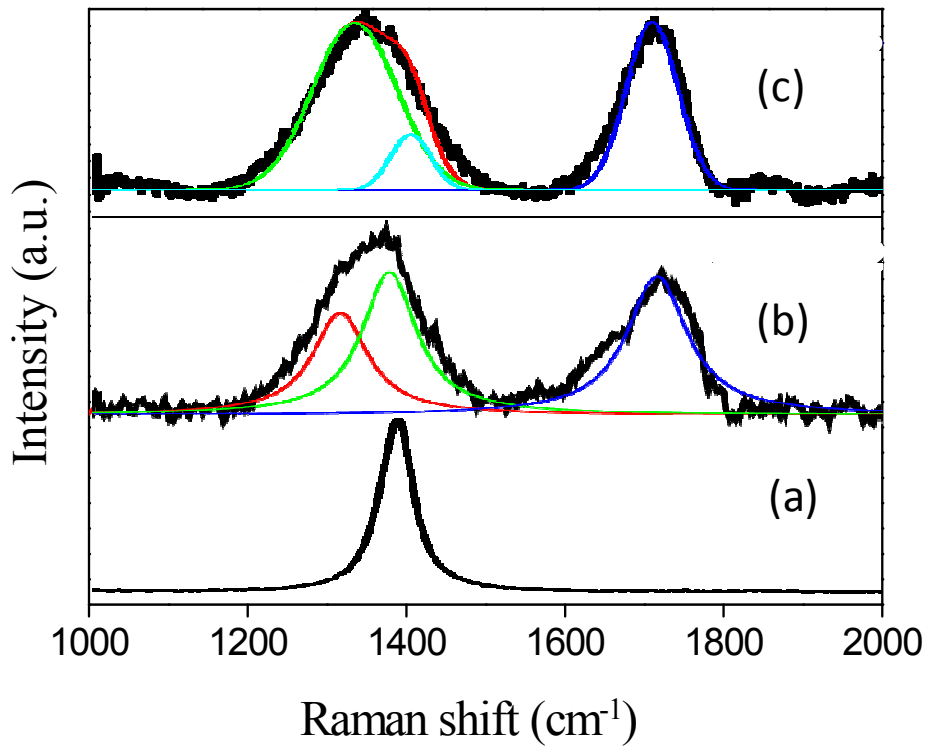

Figure 2. *Raman spectra of (a) BN (b) Physical mixture of BN/RGO*

(c) covalently attached BN/RGO

3.3.4 Conclusions

We have employed a general procedure for the synthesis of BN/RGO composites by both covalent and non-covalent functionalization. The RGO/BN composites can be characterized satisfactorily by Raman spectroscopy and electron microscopy. Electron microscopy reveals the formation of homogeneous composite. Raman spectra of the composites show the peaks corresponding to both RGO and few-layer BN. These composites may find potential application in field effect transistors.

3.4 References

1. P. F. J. Harris, Inter. Mater. 2004 (49) 31

2. E. T. Thostenson, Z. Ren, T. W. Choua, Compos. Sci. Technol. 2001 (61) 1899.

3. . P. M. Ajayan, O. Stephan, C. Colliex, D. Trauth, Science 1992 (265) 1212.

4. R. Andrews, M. C. Weisenberger, Current Opinion in Solid State and Material Science 2004 (8) 31.

5. R. H. Baughman, A. A. Zakhidov, W. A. De Heer, Science. 2002 (297) 787.

6. a) C. Downs, J. Nuget, P. M. Ajayan, D. J. Duquette, K. S. V. Santham, Adv. Mater. 1999 (11) 1028.

    b) B. Das, K. Eswar Prasad, U. Ramamurty, C. N. R. Rao, Nanotechnology. 2009 (20) 125705

7. G. B. Blanchet, C. R. Fincher, F. Gao, Appl. Phys. Lett. 2003 (82) 1290.

8. M. Cochet, W. K. Maser, A. M. Benito, M. A. Callejas, M. T. Martinez, J. Benoit, J. Schreiber, O. Chauvet, Chem. Comm. 2001 1450.

9. H. Zengin, W. Zhou, J. Jin, R. Czerw, D. W. Smith Jr., L. Echegoyen, D. L. Carroll, S. H. Fougler, J. Ballato, Adv. Mater. 2002 (14) 1480.

10. X. Zhang, J. Zhang, R. Wang, T. Zhu, Z. Liu, Chem Phys Chem 2004 (5) 998.

11. S. R. C. Vivekchand, K. C. Kam, G. Gundiah, A. Govindaraj, A. K. Cheetham, C. N. R. Rao, J. Mater. Chem. 2005 (15) 4922.

12. H.Li, Z. Xin, Q. Zhang, H. Zhang, small. 2012 (8) 682.

13. T. Wang, W. Liu, J. Tian, X. Shao, D. San, Polymer Composites 2004 (25) 111.

14. A. G. Macdiarmid, Angew. Chem. Int. Ed. 2001 (40) 2581.

15. H. S. S. R. Matte, U. Maitra, P. Kumar, B. G. Rao, K. Pramoda, C. N. R. Rao, Z. Anorg. Allg. Chem. 2012 (15) 2617.

16. C. Fite, Y. Cao, A. J. Heeger, Solid Stat. Commun. 1989 (70) 245.

17. J. Yan, T. Wei, B. Shao, Z. Fan, W. Qian, M. Zhang, Carbon. 2010 (48) 487.

18. A. G. Macdiarmid, A. J. Epstein, Faraday Discuss. Chem. Soc. 1989 (88) 317.

19. C. Valles, P. Jimenez, E. Mu. A. M. Benito, W. K. Maser, J. Phys. Chem. C. 2011 (115) 10468.

20. W. S. Huang, A. G. Macdiarmid, Polymer. 1993 (34) 1833.

21. S. G. Pawar, S. L. Patil, A. T. Mane, B. T. Raut, V. B. Patil, Archives of applied science research. 2009 (2) 109.

22. M. C. Bernard, A. Hugot-le Goff, Electrochim. Acta. 2006 (52) 595.

23. R. Mazeikiene, V. Tomkute, Z. Kuodis, G. Niaura, A. Malinauskas, Vib. Spectrosc. 2007 (44) 201.

24. Y. Furukawa, F. Ueda, Y. Hyodo, I. Harada, T. Nakajima, T. Kawagoe, Macromolecules. 1998 (21) 1297.

25. R. V. Salvatierra, M. M. Oliveira, A. J. G. Zarbin. Chem. Mater. 2010 (22) 5222.

26. M. Cochet, W. K. Maser, A. M. Benito, M. A. Callejas, M. T. Martinez, J. Benoit, J. Schreiber, O. Chauvet, Chem. Comm. 2001 1450.

27. R. Tenne, L. Margulis, M. Genut, G. Hodes, Nature 1992 (360) 444.

28. R. R. Aering. J. A. R. Stiles, K. Brandt, US Patent. 1980 4224390.

29. C. Q. Feng, J. Ma, H. Li, R. Zeng, Z. P. Guo , H. K. Liu, Mater. Res. Bull. 2009 (44) 1811.

30. Q. Xiang, J. Yu, M. Jaroneic, J. Am. Chem. Soc. 2012 (134) 6575.

31. K. Chang, W. Chen, Chem. Commun. 2011 (47) 4252.

32. W. S. Hummers, R. E. Offeman, J. Am. Chem. Soc. 80 (1958) 1339.

33. K. S. Subrahmanyam, S. R. C. Vivekchand, A. Govindaraj, C. N. R. Rao J. Mater. Chem. 2008 (18) 1517.

34. I. Calizo, A. A. Baladin,W. Bao, F. Miao, C. N. Lau, Nano lett. 2007 (7) 2645.

35. C. N. R. Rao, H. S. S. R. Matte, K. S. Subrahmanyam, Acc. Chem. Res. 2013 (46) 149.

36. C. N, R, Rao, A. K. Sood, R. Voggu, K. S. Subrahmanyam, J. Phys. Chem. Lett. 2010 (2) 572.

37. A. Nag, K. Raidongia, K. P. S. S. Hembram, R. Datta, U. V. Waghmare, C. N. R. Rao, ACS nano. 2010 (3) 1539.

38. C. Zhi, Y. Bando, C. Tang, S. Honda, K. Sato, H. Kuwahara, D. Goldberg, Angew. Chem. Int. Ed. 2005 (44) 7932.

39. C. Zhi, Y. Bando, C. Tang, S. Honda, K. Sato, H. Kuwahara, D. Goldberg, Angew. Chem. Int. Ed. 2005 (44) 7929.

CHAPTER 4

SINGLE-WALLED CARBON NANOHORNS

4.1 Synthesis, characterization and solubilization of Single-walled carbon nanohorns

Summary

Single-walled carbon nanohorns (SWNHs) have been synthesized by sub-merged arcing in liquid nitrogen. Solubilization in organic solvents has been accomplished through covalent functionalization, involving the attachment of long-chain alkyl derivative through amide bond. Water-soluble SWNHs has been produced by extensive acid treatment. Non - covalent modification of SWNHs has been done through π-π interaction by using tetrapotassium salt of coronene carboxylic acid, which gives stable dispersions in water. Interaction of SWNHs with surfactants such as polyoxyethylene-40-nonylphenyl ether (IGPAL), sodium dodecyl sulfate (SDS) and cetyl trimethyl-ammonium bromide (CTAB) produced stable aqueous dispersions, IGPAL and CTAB are effective even at low concentrations.

4.1.1 Introduction

Carbon based nanomaterials like graphene, carbon nanotubes (CNTs) and fullerenes are the materials of immense interest [1, 2a, b]. Composites of these materials exhibit remarkable enhancement in electrical and mechanical properties [3]. Among these carbon based nanomaterials, single-walled carbon nanohorns (SWNHs) are of particular interest because of their high surface area and high porosity. SWNHs are closed at one end with a conical cap [4] and have a diameter of 2-5 nm [5], unlike single-walled carbon nanotubes (SWNTs), SWNHs usually consist of spherical aggregates with diameter of 50-100 nm [6]. Although Harris *et al.* [7] first reported SWNHs sheath aggregates, Iijima *et al.* [8] synthesized in sizable quantities (50 g h^{-1}) using laser ablation of graphite in He or Ar atmosphere. It may be noted that no catalyst is required for the synthesis of highly pure SWNHs unlike SWNTs. Morphologically SWNHs are of three kinds (a) dahlia flower (b) bud and (c) seed like aggregates [9]. Dahlia-like aggregates posses long cone-shaped tips with cone angles of 20° which can be clearly visible at the surface of the spheres. In case of bud and seed-like aggregates there are no protruding horns at the surface of the spheres and the nanotube structure appear to be shorter.

Recent reports show SWNHs are most promising candidates for hydrogen and methane storage as well as for drug delivery applications [11-12]. Most of the biological process takes place in solution phase. But unfortunately, SWNHs in their pristine form insoluble in most of the solvents. Functionalization is the most accessible route to enhance solubility [13]. Chemical modification of the surface is expected not only introduce desired

solubility but also contribute to the study of their solution properties. In order to make SWNHs dispersion in various solvents, it is necessary to physically or chemically attach proper functional groups without altering its desirable properties. In past decade, plenty of investigation has been carried out on functionalization of SWNTs, where as for SWNHs funtionalization and solubilization, much research has not been carried out except the very few reports, which includes covalent attachment of organic fragments and non-covalent functionalization. Covalent functionalization involves direct nucleophilic addition of monoprotected diamine via carbonyl group of oxidized SWNHs [13]. Non-covalent functionalization is achieved by π-π stacking interactions with conjugated aromatic molecules like pyrene [14].

Charge transfer interaction of carbon based materials with various electron-donors and -acceptors are well reported in literature. The interaction of electron-donors and -acceptors with graphene and SWNT has been well characterized by using Electronic absortion, Raman spectroscopy as the main techniques [17]. It has been observed that electron-acceptor molecules will interact strongly with graphene as compare to electron-donor molecules [18]. Interestingly, it was observed that aromatic conjugated systems like coronene salt will not only help to solubilize the graphene but also show significant charge transfer through its π-π interaction. We have also carried out similar experiments of SWNHs with tetrapotassium salt of coronene carboxylic acid (CS) and investigated their properties. It may be noted that there is enhancement in the solubility of SWNHs in aqueous medium along with significant charge transfer interaction.

We have carried out functionalization of SWNHs by employing both covalent and non-covalent means. The functionalized samples were characterized by employing Infrared (IR) spectroscopy, Scanning electron microscopy (SEM) and Raman spectroscopy. The covalent functionalization has been carried out through the following two independent routes (a) acidification followed [18] by (b) amidation. Amidation makes SWNHs soluble in organic solvents like THF and CCl_4. Acidification of SWNHs gives aqueous dispersions, which are stable up to week. While non-covalent functionalization attained through (a) π-π interaction and (b) supramolecular approach using surfactants. supramolecular approaches give stable aqueous dispersions which are stable for several days.

4.1.2 Experimental section

SWNHs Synthesis

The submerged arc method was used for the preparation of SWNHs as reported in the literature [19]. Briefly DC-arc discharge was generated between two graphite electrodes submerged in liquid nitrogen in a stainless steel dewar. The arc discharge was initiated inside the liquid nitrogen by touching a 99.99% purity graphite anode (6 mm in diameter) with a graphite cathode (12 mm tip diameter) of similar purity. The applied DC-arc voltage and currents were 35 V and 65 A respectively. The gap between the electrodes kept constant at around 1 mm by continuously translating the anode during the experiment in order to maintain a stable discharge. The arc discharge in liquid nitrogen was turbulent. After arcing, remaining liquid nitrogen was transferred from dewar to a glass beaker and allowed it to

evaporate. The product settled at the bottom of dewar was also collected. Figure 1, shows the schematic diagram of experimental set-up used for production of SWNHs by sub-merged arcing technique. In figure 2 we show the photographs taken during arcing.
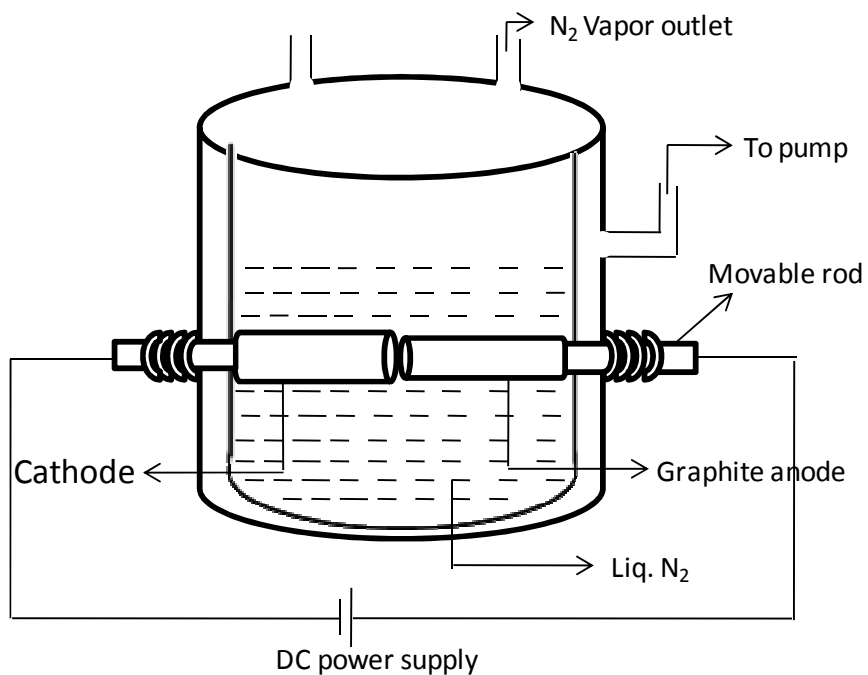

Figure 1. *Schematic diagram of the experimental set-up.*

Figure 2. *Photographs taken during arcing.*

Amidation

To solubilize SWNHs in non polar solvents, amidation has been carried out. The procedure is has follows. In the first step, conc. nitric acid (2 ml), conc. sulphuric acid (2 ml) and water (16 ml) was added to SWNHs (50 mg) and subsequently heated in a microwave oven in a teflon-lined stainless steel autoclave for 10 minutes. Further, the sample was heated at 100 ^{o}C for 12 hrs under hydrothermal conditions. The product was washed with distilled water and centrifuged repeatedly to remove traces of the acid. The as synthesized SWNHs was functionalized with –OH and –COOH groups. The acid treated SWNHs were refluxed with excess $SOCl_2$ for 12 hrs and the unreacted $SOCl_2$ was removed under vacuum. The product was treated with dodecylamine (DDA, 5 ml) under microwave irradiation for 10 minutes and finally heated at 100 ^{o}C for 12 hrs.

Functionalization through π-π interaction

To an 10 ml aqueous solution of coronene salt (concentration 1mg/ml), 5 mg of as synthesized SWNHs was added and dispersed for few minutes with sonication followed by refluxing at 100 °C for 24 h. Subsequently, mixture was further sonicated at 70 ^{o}C for 2 h. After cooling to room temperature the resulting mixture was centrifuged to give a black transparent solution [20].

Supramolecular approach

To get stable aqueous dispersions of SWNHs, we prepared different concentrations of surfactant solutions and checked for dispersibility. The procedure is as follows; 1.5 mM, 3 mM, 6 mM and 9 mM solutions of CTAB (cetyl trimethyl ammonium bromide), IGPAL (polyoxyethylene-40-nonylphenylether) and SDS (sodium dodecyl sulfate) were prepared individually. To 5 ml of each of these solutions, 1 mg of SWNHs was added and ultrasonicated for 15 minutes to obtain dispersions.

4.1.3 Results and discussion

We have prepared SWNHs by employing arc evaporation of graphite rod in liquid nitrogen temperature. We have investigated the quality of samples by employing different characterization techniques such as FESEM, TEM, Raman and IR, X-ray photoelectron spectroscopy.

In Figures 3a and b we show the TEM and FESEM images of SWNHs containing spherical clusters, sizes in the range of 60-100 nm. Figure 3c shows the FESEM images contain spherical SWNH particles, produced (having similar morphology) under similar condition. Figure 3d shows TEM images of SWNHs which has both bud and dahlia kind morphology, the corresponding high resolution image indicates the horn formation in SWNHs structure.
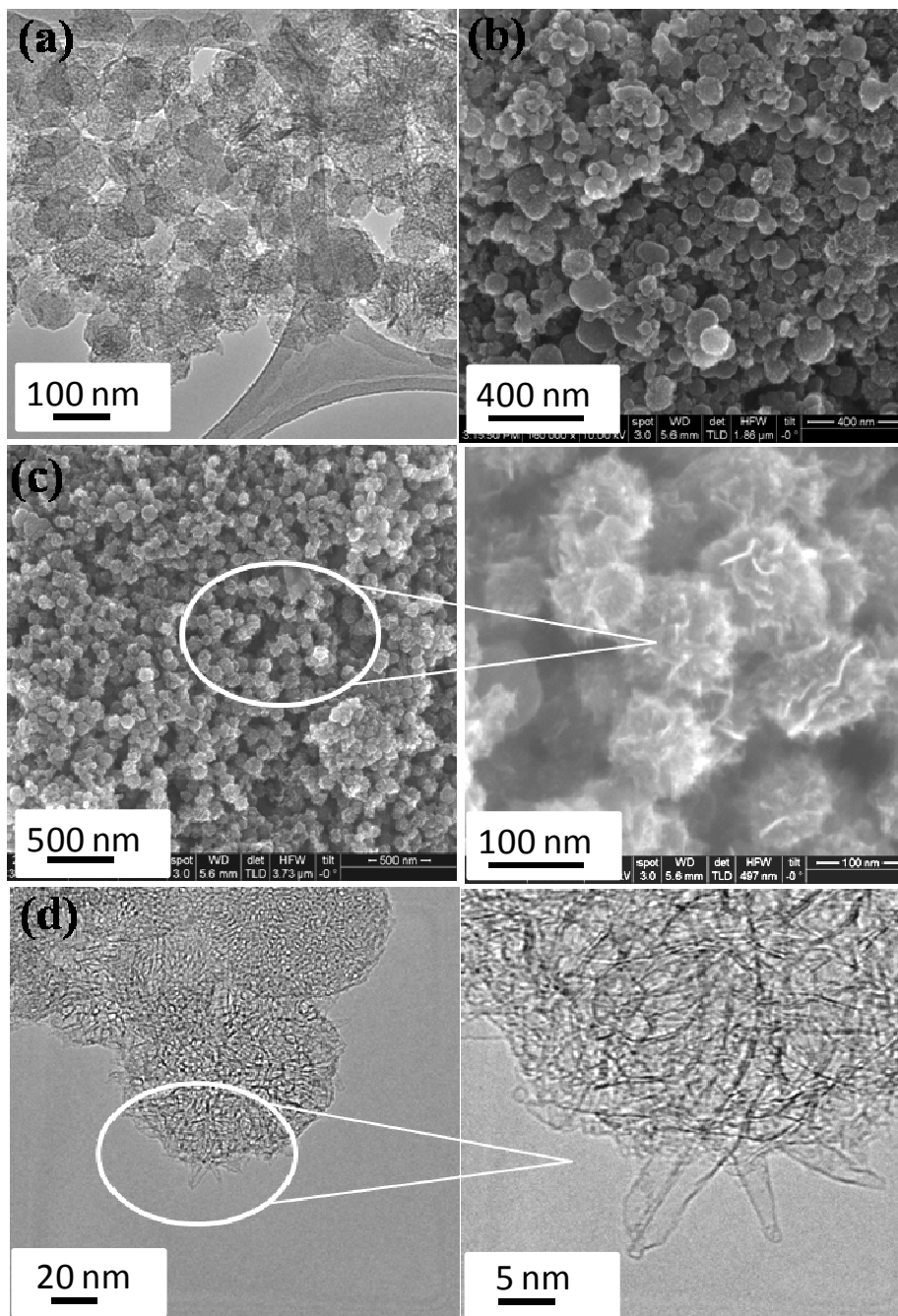
Figure 3. *(a) TEM, (b) and (c) FESEM (D) HRTEM images of SWNHs.*

X-ray photoelectron spectroscopic (XPS) analysis showed that SWNHs prepared by uscontained 1.5 at% nitrogen. In Figure 4a we show typical core level XPS spectra of C 1s signal ranging from 283 to 290 eV. Asymmetric nature of the peak reveals presence of more than on kind of carbon in our system. On deconvolution we find peaks at 284.2, 285.6 and 287.6 eV corresponding to C-C, C=N and C-N bonds respectively. Appearance of C-N band confirms the doping of nitrogen in SWNHs. In Figure 4b we showed XPS spectra of N 1s signal ranging from 397 to 403 eV. The asymmetric shape of the N 1s peak indicates the existence of more than one component. The specific binding energy values 398.2, 400.3 and 402 eV corresponding to pyridinic, pyrrolic and quaternary nitrogen respectively.
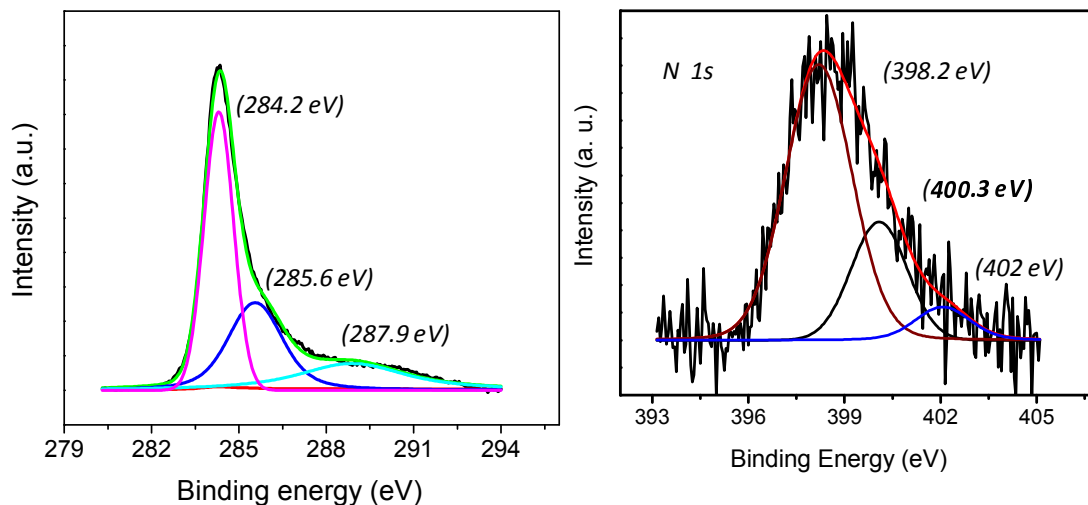

Figure 4. *(a) C 1s and (b) N 1S XPS signals of SWNHs.*

We have recorded the Raman spectra at different locations of the sample by employing 632.8 He-Ne laser. In Figure 5a we show typical Raman spectra of SWNHs. It shows two prominent bands around 1350 cm^{-1} corresponding to D-band and 1590 cm^{-1} corresponding to G-band along with 2D-band around 2300 cm^{-1}. UV-Vis spectra show maxima at 270 nm due to π-$\pi*$ transition.
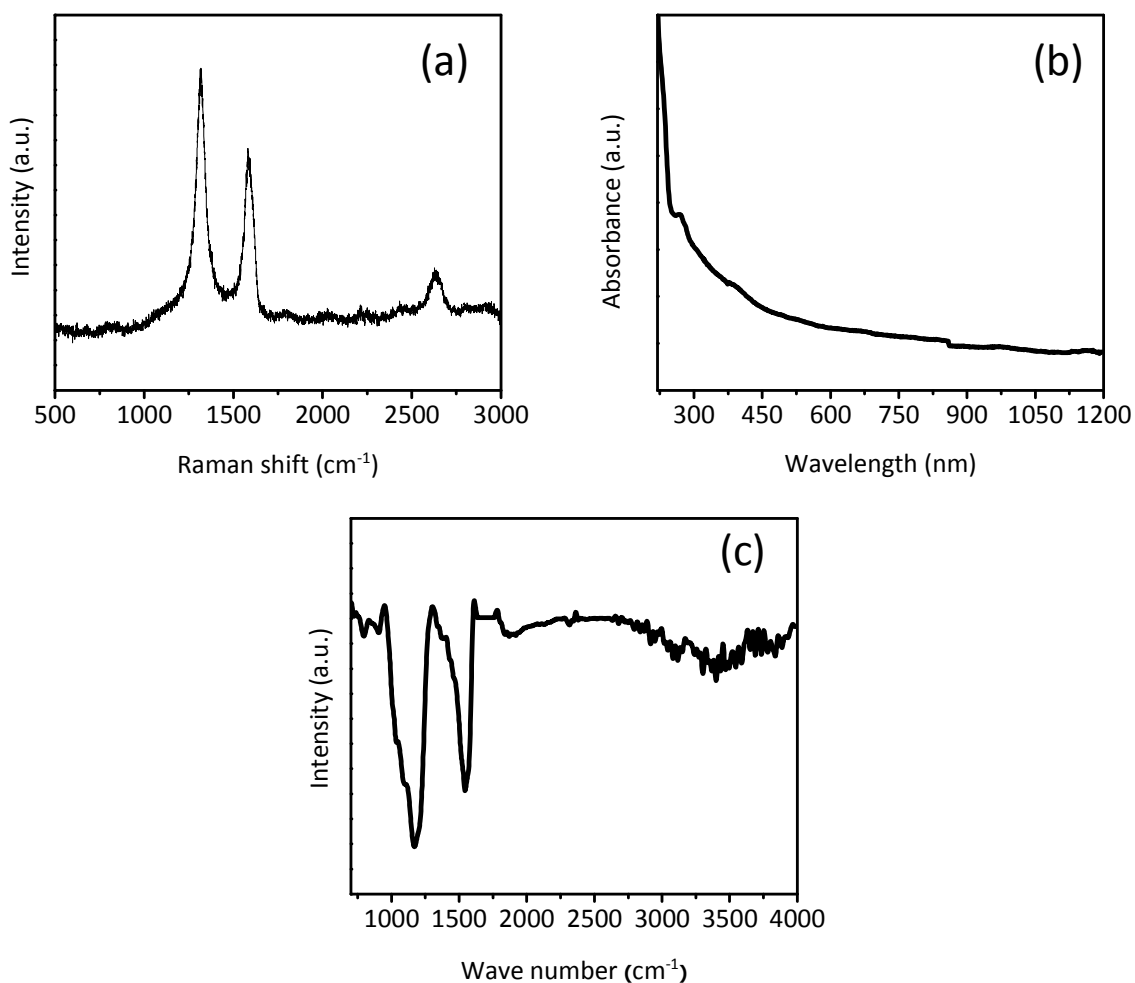
Figure 5. *(a) Raman (b) UV-Vis and (c) IR spectrum of SWNHs.*

Acidification

As prepared SWNHs produced by arcing technique shows evidence of the peaks corresponds to C=C and hydroxyl groups on the surface. After treatment of SWNHs with nitric and sulphuric acid mixture, we obtained water soluble SWNHs (SWNHs-COOH), along with the water insoluble portion, which settles down. The infrared (IR) spectrum of the soluble part obtained after drying shows a prominent band due to carbonyl group at 1720 cm^{-1} (Figure 6). Interestingly, this prominent carbonyl peak is absent in the pristine SWNH sample as shown in Figure 5c.
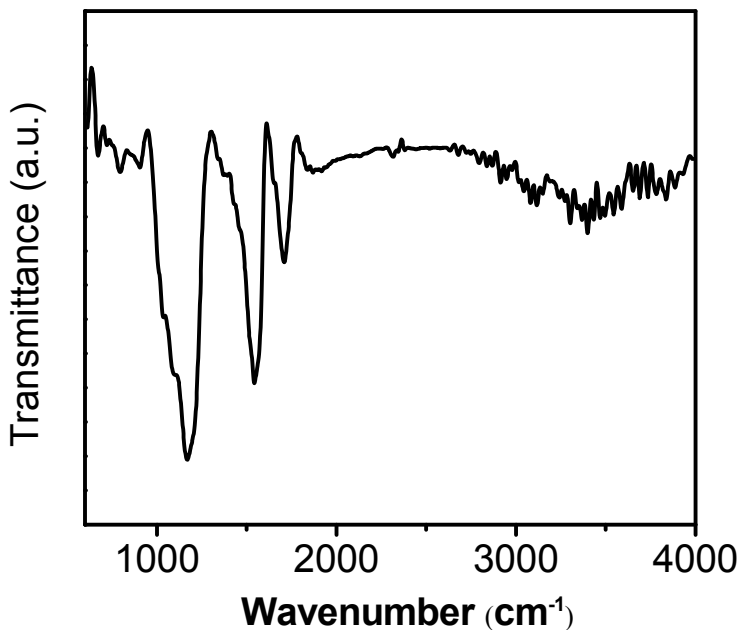

Figure 6. *IR spectrum of acid functionalized SWNHs.*

Raman spectrum of the water soluble SWNHs is shown in Figure 7a exhibits characteristic G, D and 2D band. We have observed that the D-band intensity is increased with respect to G-band in the case of oxidized SWNHs (Figure 7a), compared to as prepared SWNHs. In Figure 7b, we show photograph of water soluble SWNHs.
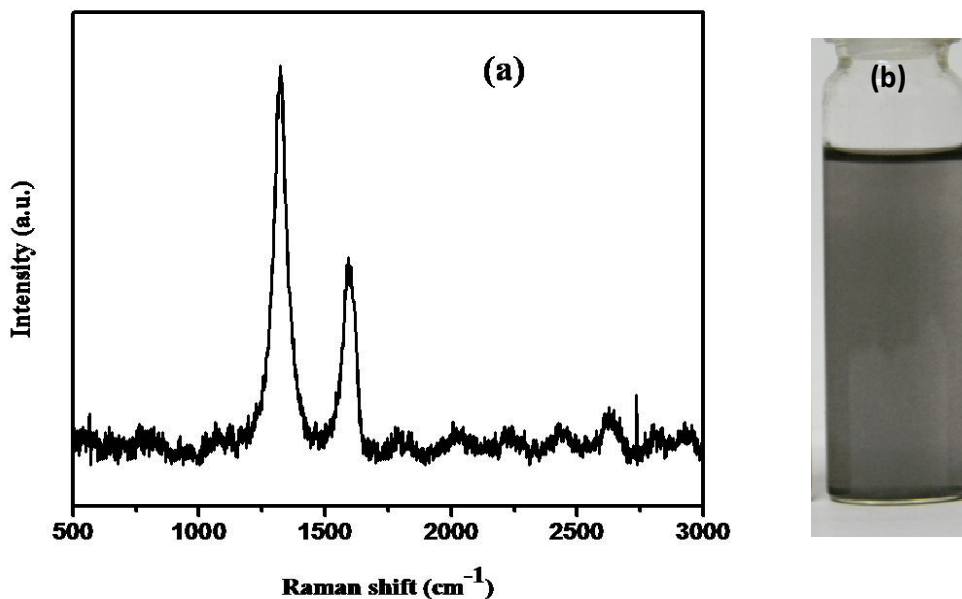
Figure 7. *(a) Raman spectrum (b) water dispersions of the acid functionalized SWNHs.*

Amidation

Amidation reaction for SWNHs is carried out in a similar way as reported for carbon nanotubes (page 82). After amide functionalization stable dispersions of SWNHs in various non polar solvents were obtained. Our observation is similar to the report from Haddon and co-workers [21]. In Figure 8 we show photographs of the dispersions of functionalized SWNHs in tetrahydrofuran and carbon tetrachloride. The solubility of product is 0.5 mg/ml.
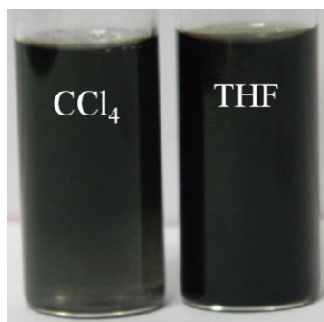

Figure 8. *Dispersions of the SWNHs-DDA in different solvents.*

Figure 9 shows the IR spectra of SWNHs-COOH and SWNHs-DDA. Functionalization of SWNHs through amide bond is evidenced by IR spectrum. SWNHs-COOH shows stretching at 1720 cm^{-1} corresponding to C=O stretching of carboxylic acid group, which shifts to higher frequency in the corresponding acyl chloride derivative. The spectrum of SWNHs-DDA shows two peaks at 1572 and 1639 cm^{-1} which are the respective characteristic frequencies of –NH bending and C=O stretching of the amide group. In addition we have observed C-H stretching band around 2800 cm^{-1}.
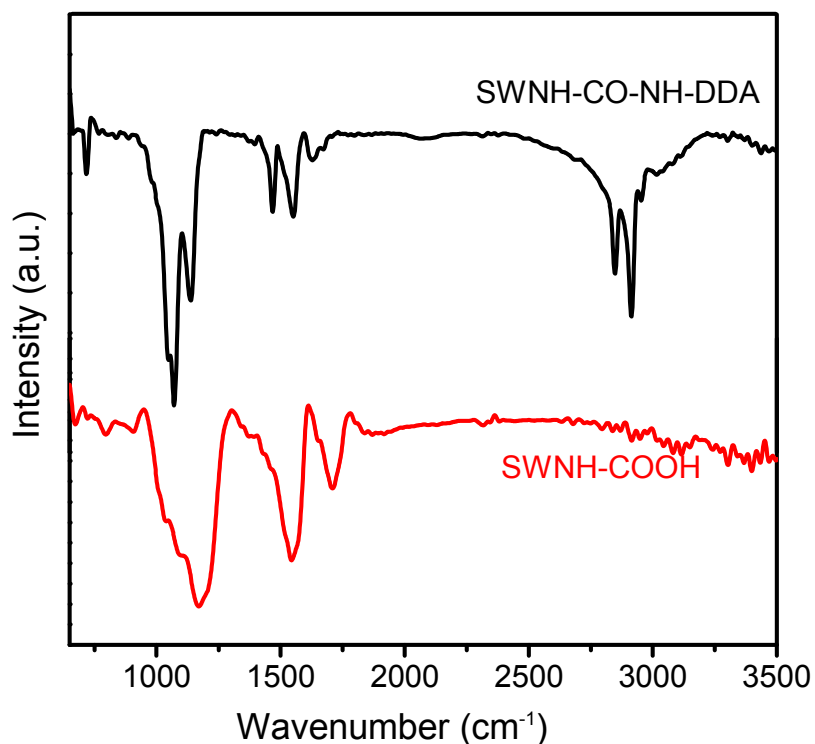

Figure 9. *Infrared spectra of acid treated SWNHs (SWNH-COOH) and amide functionalized SWNHs (SWNH-CO-NH-DDA)*

95

Functionalization through π-π interaction

The SWNHs, obtained by arcing in liquid nitrogen temperature are used to study the non-covalent interaction with coronene salt (CS). In the present study we have chosen an anionic derivative of coronene for non-covalent functionalization. Coronene is the simplest six-fold symmetrical aromatic molecule after benzene. It is a blue fluorescent material and its derivatives, in the form of esters and imides are known to be liquid crystalline with high fluorescence emission in solution as well as in the solid state [22, 23]. Although coronene is electron rich, its imide and carboxylate derivatives are known to be electron diffiecient [22-24].

We have been able to accomplish the solubilization of SWNHs in water by reacting with CS. It was necessary to reflux and sonicate SWNHs with CS in order to obtain stable aqueous dispersions. Ultrasonication expected to overcome the Van der Wall's interactions between the aggregated SWNHs. Moreover anionic CS is also assisting in stabilizing the exfoliated SWNHs. The mixture was then centrifuged to remove the insoluble SWNHs, which might have not fully exfoliated. The aqueous solutions are stable for months, indicating efficient solubilization. The presence of SWNHs in the aqueous phase was confirmed by Raman spectroscopic technique. The dark-black color of the SWNHs-CS dispersions suggests that CS is more efficient in solubilizing in SWNHs. By measuring the weight of the centrifuged residue, the concentration of the SWNHs solubilized in water is estimated to be 0.15 mg/ml.

Coronene has a very large planar aromatic surface that permits strong interaction with the SWNHs surface through synergistic noncovalent charge-transfer and π-π stacking interactions. Furthermore, negative charge of CS prevents both inter and intra π-π stacking of SWNHs, which leads to the solubilization of the functionalized SWNHs. Therefore, this design strategy has enabled us to obtain highly stable aqueous dispersions. To investigate the changes in the optical properties we have carried out detailed studies of these samples. Figure 10a shows the absorption spectra of CS and SWNHs-CS of varying ratio.
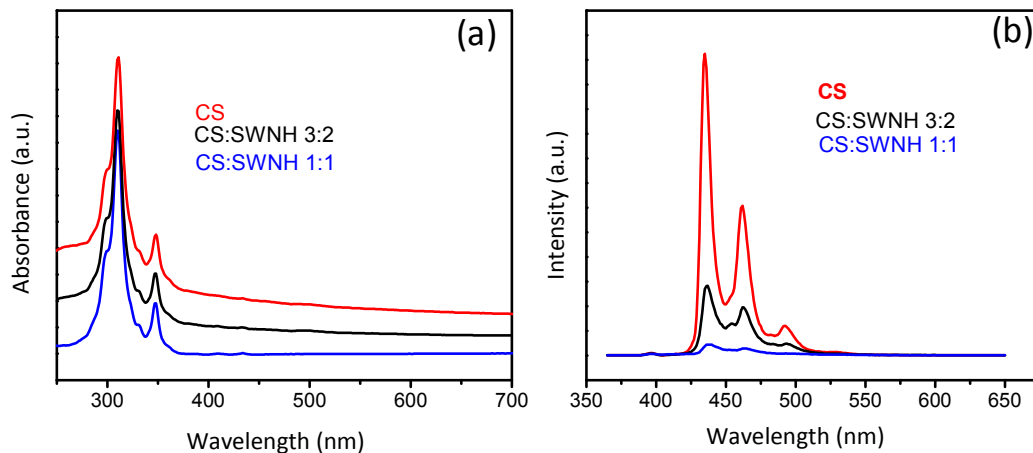

Figure 10. *(a) Absorption (b) Fluorescence spectra of SWNHs-CS*

The electronic absorption band of CS in presence of SWNHs indicates that there is no significant ground state charge transfer interaction whereas the excited state charge transfer interaction was evidenced from the fluorescence spectra shown in Figure 10b. The PL spectra of CS show remarkable change after the addition of SWNHs. It is speculated that the strong quenching of fluorescence may be due to an excited state charge transfer.

Chapter 4.1

We have carried out detailed Raman measurements to further investigate the mode of charge-transfer interactions in composites (Figure 11). The Raman G band of graphene is known to soften or stiffen due to interaction with electron-donor and -acceptor molecules respectively. By comparing the G bands of SWNHs and SWNHs-CS films, it is evident that the G band of SWNHs-CS (1590 cm^{-1}) composites stiffens by 13 cm^{-1} (In case of 3:2 composites of CS:SWNHs). The significant stiffening in G band confirms charge transfer interaction between CS and SWNHs as indicated by PL spectra.
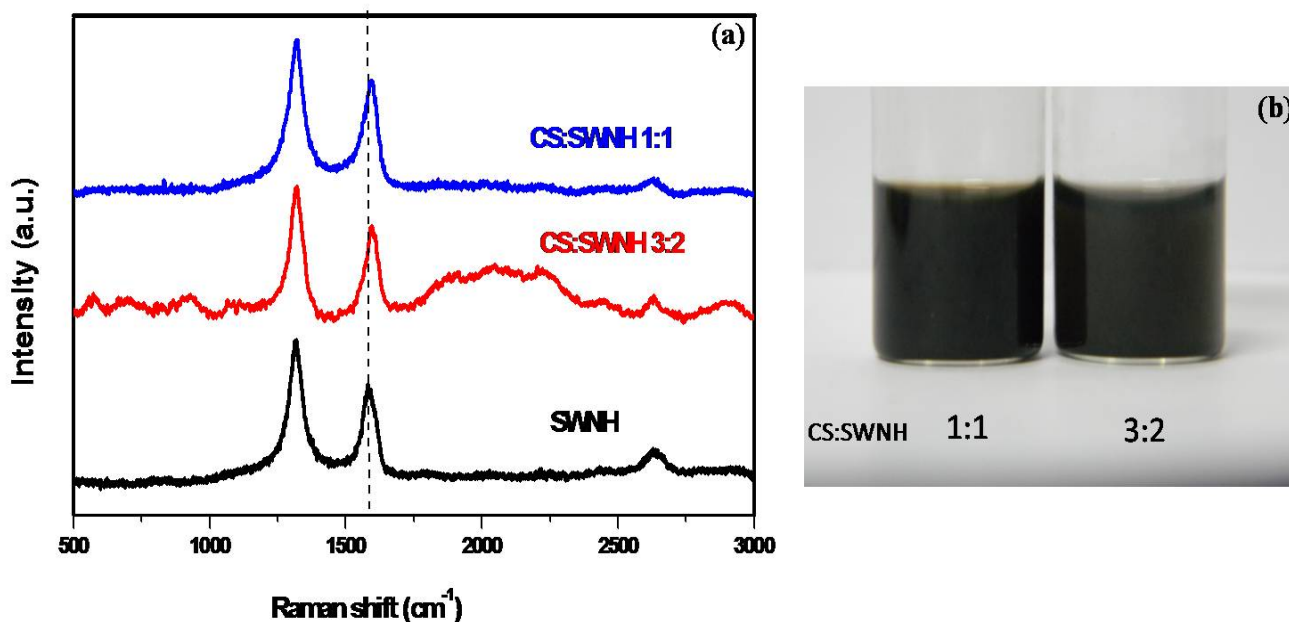

Figure 11. *(a) Raman spectra of SWNH (black) CS: SWNH 3:2 (red) CS: SWNH 1:1 (blue) (b) Dispersions of SWNHs-CS in water.*

Supramolecular approach

Non-covalent functionalization was carried out via supramolecular approach by using different concentrations of various surfactants such has CTAB, SDS and IGP. In the case of CTAB and IGP, the best dispersion was obtained at 3 mM, whereas in case of SDS we got better dispersions at slightly higher concentration of 6 mM. Photographs of the SWNHs dispersions in different surfactants are shown in Figure 12.
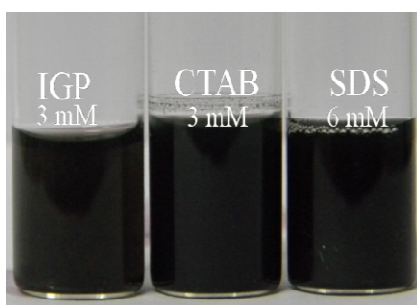

Figure 12. *Dispersions SWNHs in surfactants.*

Small aggregates of SWNHs obtained after treating with surfactant IGP is shown in FESEM images (Figure 13).
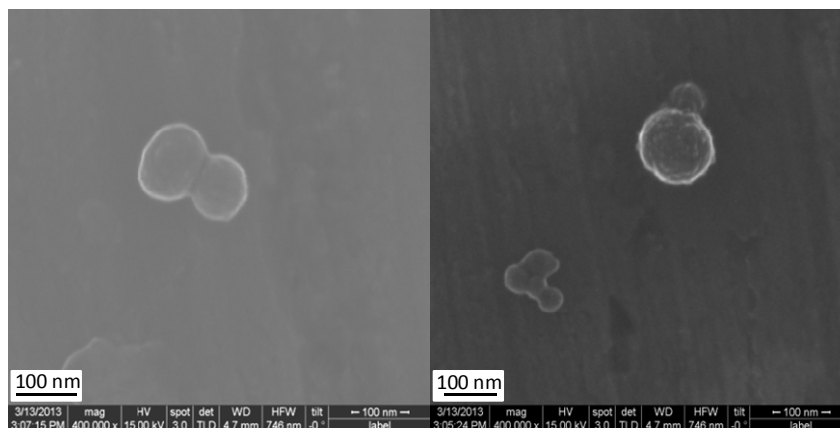

Figure 13. *FESEM images of SWNHs dispersed in IGP*

4.1.4 Conclusions

Submerged arc-discharge in liquid nitrogen can be conveniently used for the continuous production of SWNHs. The SWNHs so prepared contain 1.5 at % nitrogen. We have been able to functionalize and solubilize SWNHs by employing covalent, non-covalent functionalization as well as treating with surfactants. Solubilization in non-polar solvents has been accomplished through covalent functionalization using long chain alkyl amine. We have shown a simple way to obtain stable aqueous dispersions by non-covalent functionalization, using coronene salt. SWNHs-CS composites shows charge transfer interactions because of π-π interaction. Optical and Raman spectroscopy were used as the techniques to characterize electronic charge transfer. Thus our approach to functionalize SWNHs non-covalently is not only applicable for increase in the processability but also we can tune the electronic properties through molecular charge-transfer. Microscopic studies reveal the formation of small SWNHs aggregates after treating with surfactants. Aqueous dispersions of surfactant stabilized SWNHs were stable upto month.

4.2 Boron and nitrogen doped Single-walled carbon nanohorns

Summary

Doping is a common approach to tailor electronic properties of the semiconductor materials. Moreover, doping graphene by heteroatoms such as nitrogen and boron is the subject of research because of their ability to open the band gap, which in turn will alter local electronic and chemical structure. Electrochemical and molecular charge transfers are the well known methods to dope carbon based materials. Marked changes in the Raman spectrum of carbon based materials is observed after doping. Interestingly, SWNHs are the structural analogues of graphene. They are the horn-shaped sheath aggregate of graphene sheets. Here, we have reported a new technique to dope SWNHs by both nitrogen and boron. Our technique is based on arc-discharge of graphite electrodes in liquid nitrogen medium. To dope nitrogen and boron we have used melamine and boron-stuffed graphite electrodes as the precursors. Doped samples were characterized by XPS and Raman spectroscopy. G-band in the Raman spectrum of SWNHs is stiffens after B and N-doping with intensification of D-band.

4.2.1 Introduction

Tuning physiochemical properties of carbon based material becomes necessary in many applications [25]. One way of achieving this control is by elemental doping, a method effectively used in semiconductor silicon technology. For example, nitrogen atoms in silicon lock dislocations to increase mechanical strength [26]. Effects of doping silicon with phosphorous and other elements with different oxidation states have been well documented. Chemical substitution brings about significant changes in carbon materials as well. In particular, substitution of boron or nitrogen in carbon nanostructures render them p or n-type respectively [27]. Besides the electronic structure, doping affects the Raman spectra and other properties of carbon nanostructures [25].

Different routes have been reported to dope carbon nanotubes (CNTs). Substitution of carbon by nitrogen in multi-walled carbon nanotubes (MWNTs) was achieved by the pyrolysis of aza aromatics (pyridine, triazine) [28]. The nitrogen content decreased with increase in temperature of pyrolysis, the estimated nitrogen content being around 5, 3.5 and 3 at.% in nanotubes prepared by the pyrolysis of pyridine at 973, 1123 and 1723 K respectively. Boron-doped MWNTs prepared by the pyrolysis of acetylene-diborane mixtures in a stream of helium and hydrogen [29]. Boron and Nitrogen doped graphene have been prepared by the arc-discharge of graphite electrodes stuffed with boron and melamine respectively [30]. N-doping is known to improve the performance of graphene electrode as supercapacitors [31]. Doping effects are ideally monitored by Raman spectroscopy. B- and N- doped graphene show stiffening of G-band [30]. SWNHs are structural analogues of graphene; one can speculate similar electronic and spectral changes after doping. With this

motivation we prepared B- and N-doped SWNHs. We employed DC-arc discharge between carbon electrodes in liquid nitrogen. Cathode is pure graphite electrode and anode is stuffed with boron or melamine. Doped samples were characterized by various physical techniques such as Raman, XPS etc. Here, boron and nitrogen doped SWNHs are designated as B-SWNHs and N-SWNHs respectively.

4.2.2 Experimental section:

Synthesis of Boron and Nitrogen doped SWNHs:

B-SWNHs was prepared by performing arc-discharge of elemental boron stuffed graphite electrodes (acting as anode) in liquid nitrogen medium (Applied DC current is of 65 A and voltage of 30 V). Similarly N-SWNHs were prepared by performing arc-discharge of melamine stuffed graphite anode in liquid nitrogen medium.

4.2.3 Results and discussion

In Figure 1 we show typical core-level X-ray electron photoelectron spectra (XPS) of N-SWNHs. XPS analysis shows nitrogen content of 5 at % (compared 1.5 at % in the absence of melamine). Asymmetric nature of the N 1s peak (Figure 1b) reveals the presence of more than one kind of nitrogen. Nature of binding between carbon and nitrogen can be predicted by analyzing binding energy values in XPS. The obtained N 1s spectrum reveal the presence of mainly three types of nitrogen, which indeed confirms the successful nitrogen doping. The specific binding energy 398.4, 399.7 and 401 eV corresponding to pyridinic, pyrrolic and quaternary N respectively [32] (Figure

1b). XPS of N-SWNHs shows predominant C 1s signal ranging from 283.5 eV to 290 eV. Asymmetric nature of the C 1s peak (Figure 1a) also reveals the presence of more than one kind of carbon in our system. The specific binding energy 284.7 and 287.6 eV corresponding to C-C and C-N bond respectively (Figure 1a) [33]. The appearance of C-N bond further confirms the doping of nitrogen in carbon matrix.
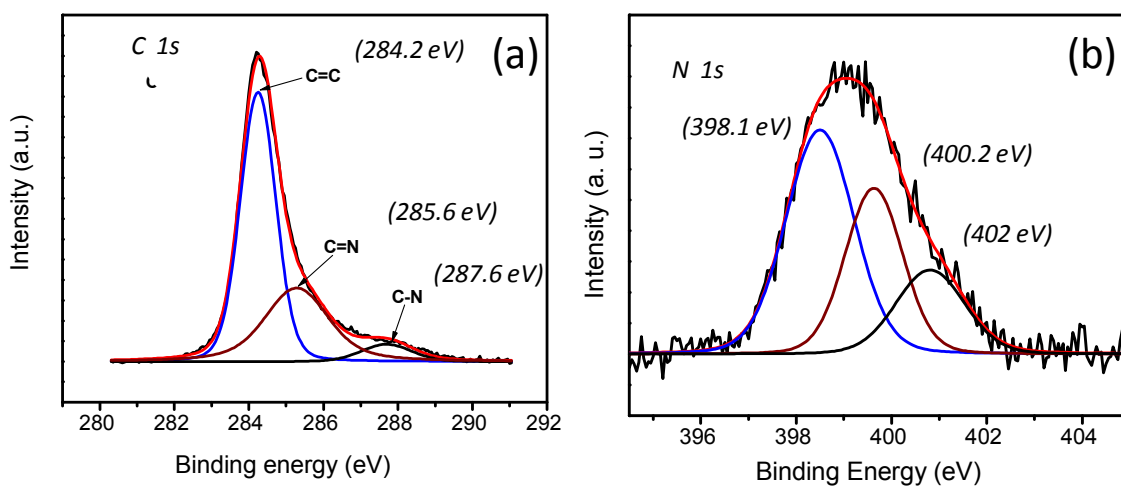
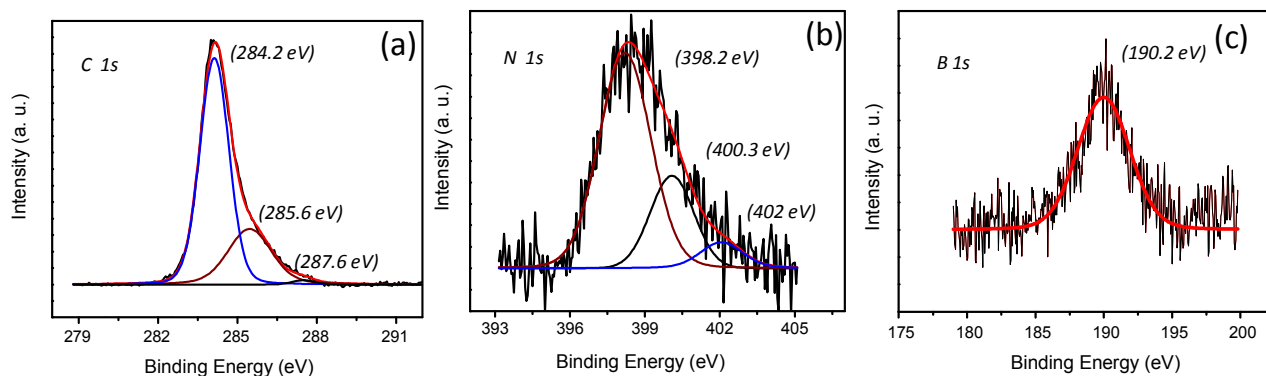**Figure 1.** *(a) C 1s and (b) N 1S XPS signals of N-SWNHS.*

Figure 2. *(a) C 1s, (b) N 1s and (c) B 1s XPS signals of B-SWNHS.*

Boron doping is confirmed by the presence of prominent signal at 190.1 eV (Figure 1c). The position of the feature indicates that boron is bonded to carbon in the sp^2 network [30]. XPS analysis showed that B-SWNHs contain 2 at % of boron. In B-SWNHs we have observed the co-doping of nitrogen, since arcing is carried in liquid nitrogen B-SWNHs contain 1.5 at% of nitrogen, shows peaks at 398.1 and 400.2 eV corresponding to pyridinic and pyrrolic nitrogen respectively (Figure 2b).

After doping there is no change in morphology of nanohorns. We have observed both bud-like and dahlia like structure in case of N-SWNHs (shown in the Figure 3).
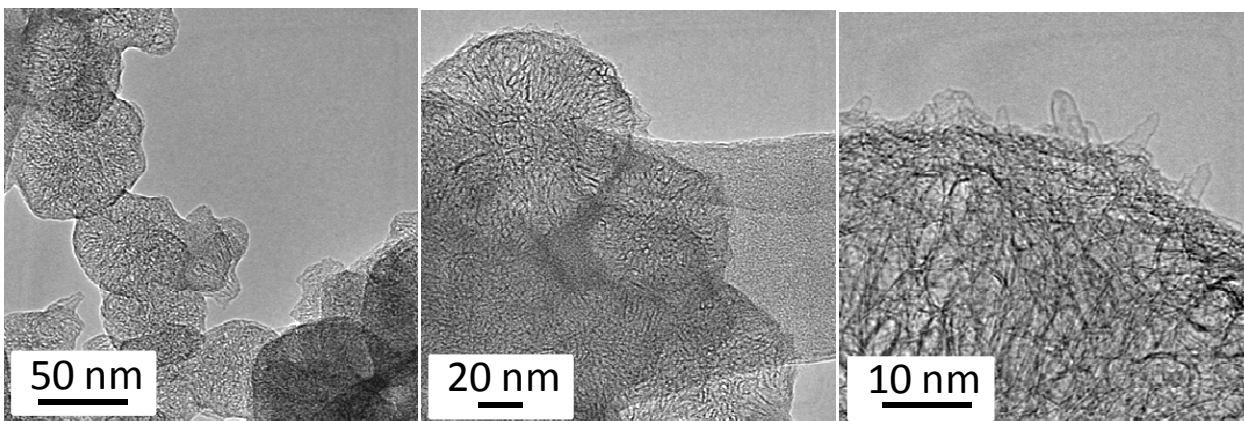

Figure 3. *TEM images N-SWNHs*

We have carried out detailed Raman study of N-SWNHs and B-SWNHs in comparison with the SWNHs (Figure 4). Three main features were observed in the Raman spectrum (excited with laser of 632.8 nm) of the samples is in the region between 1000-3000 cm^{-1}. The G-band (~ 1570 cm^{-1}), defect related D-band (~ 1320 cm^{-1}) and 2D-band (~ 2640

cm^{-1}). In the case of doped samples stiffening of G-band is observed compared to SWNHs, which is similar to the observation of electrochemical doping. Also, doped samples show higher D-band intensity as compared to parent SWNHs (Figure 4).
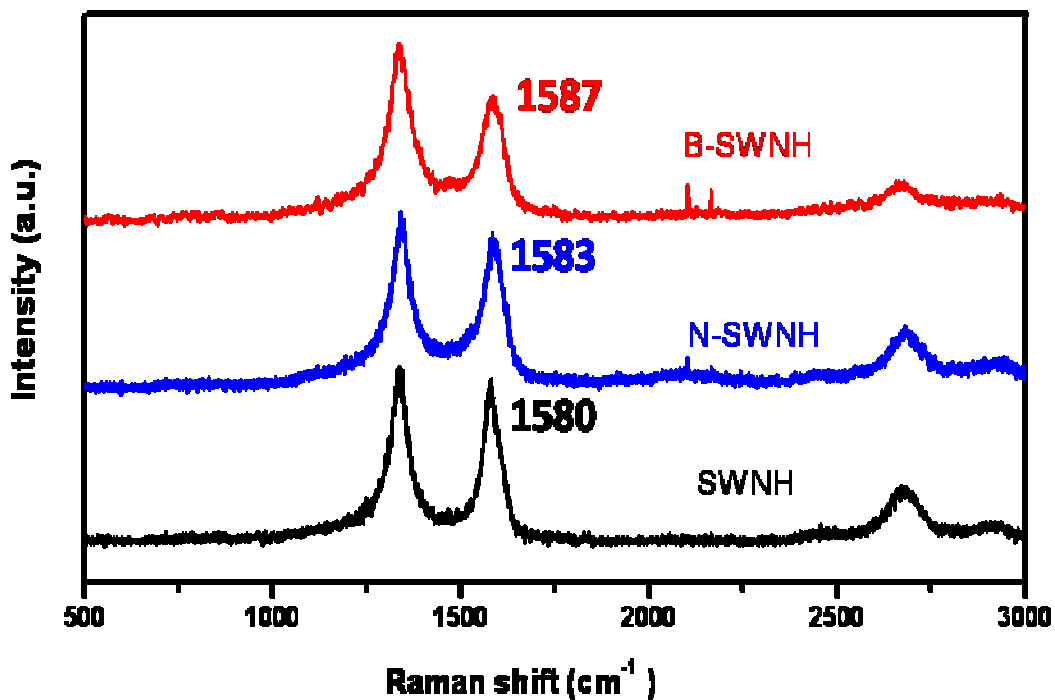

Figure 4. *Raman spectra of B- and N-doped SWNHs*

4.2.4 Conclusions

We have synthesized SWNHs by arc-discharge of graphite in liquid nitrogen and presented the possible routes for the synthesis of B and N-doped SWNHs. SWNHs can be readily doped with nitrogen or boron by carrying out submerged DC-arc discharge of composite graphite rods filled with elemental boron or melamine in liquid nitrogen medium. No change in morphology of SWNHs has been observed due to doping. Raman spectroscopy provides valuable information regarding changes in the electronic structure of carbon nanostructures after doping. Stiffening of the G-band has been observed in both B- and N-doped SWNHs. In case of elemental and electrochemical doping stiffening of graphene G-band is observed. Molecular charge transfer found to induce different effects.

4.3 References

1. C. N. R. Rao, K. Biswas, K. S. Subrahmanyam, A. Govindaraj, J. Mater. Chem 2009 (19) 2457.

2. a) S. R. C. Vivekchand, C. S. Rout, K. S. Subrahmanyam, A. Govindaraj, C. N. R. Rao, J. Chem. Sci. 2008 (120) 9.

   b) A. Govindaraj, B. C. Satishkumar, M. Nath, C. N. R. Rao, Chem. Mater. 2000 (12) 202.

3. P. F. J. Harris, Inter. Mater. Rev. 2004 (49) 31.

4. S. Utsumi, K. Uvita, H. Kanoh, M. Yudaska, K. Suenaga, F. Kokai, S. Iijima, J. Phys. Chem. B. 2006 (110) 7165.

5. V. Krunglevicute, A. D. Migone, M. Pepka, Carbon. 2009 (47) 769.

6. R. Yuge, T. Ichihashi, Y. Shimakawa, Y. Kubo, M. Yudaska, S. Iijima, Adv. Mater. 2004 (16) 1420.

7. P. F. J. Harris, S. C. Tsang, J. B. Claridge, M. L. H. Green J. Chem. Soc. Faraday. Trans. 1994 (90) 2799.

8. S. Iijima, M. Yudasaka, R. Yamada, S. Bandow, K.Suenaga, F. Kokai and K. Takahashi Chem. Phys. Lett. 1999 (309) 165.

9. T. Azami, D. Kasuya, R. Yuge, M. Yudasaka, S. Iijima, T. Yoshitake, J. Phys. Chem. C. 2008 (112) 1330.

10. Y. Zhao, J. Li, Y. Ding, L. Guan, Chem. Commun. 2011 (47) 7416.

11. K. Murata, A. Hashimoto, M. Yudasaka, D. Kasuya, K. Kaneko, S. Iijima, Adv. Mater. 2004 (16) 1520.

12. K. Ajima, M. Yudasaka, T. Murakami, A. Maigne, K. Shiba, S. Iijima Mol. Pharm. 2005 (2) 475.

13. C. Cioffi, S. Campidelli, F. G. Brunetti, M. Meneghetti, M.prato, Chem. Comm. 2006 2129.

14. J. Zhu, M. Yudasaka, M. Zhang, D. Kasuya, and S. Iijima, Nano. Lett. 2003 (3) 1239.

15. E. Dujardin, T. W. Ebbesen, A. Krishnan, M. M. J. Treacy, Adv.Mater. 1998 (10) 1472.

16. Y. Chen, S. Fang, P. C. Eklund, W. H. Lee, R. E. Smalley J. Mater. Res. 1998 (13) 2423.

17. R. Voggu, C. S. Rout, A. D. Franklin, T. S. Fisher, C. N. R. Rao J. Phys. Chem. C. 2008 (112) 13053.

18. S. Niyogi, E. Bekyarova, M. E. Itkis, J. L. McWilliams, M. A. Hamon, R. C. Haddon, J. Am. Chem. Soc. 2006 (128) 7720.

19. H. Wang, M. Chhowalla, N. Sano, S. Jia , G. A. J. Amaratunga, Nanotechnology 2004 (15) 546.

20. A. Ghosh, K. V. Rao, S. J. George, C. N. R. Rao, Chem. Eur. J. 2010 (16) 2700.

21. S. Niyogi, E. Bekyarova, M. E. Itkis, J. L. McWilliams, M. A. Hamon, R. C. Haddon, J. Am. Chem. Soc. 2006 (128) 7720.

22. S. Alibert-Fouet, I. Seguy, J. –F. Bobo, P. Destruel, H. Bock, Chem. Eur. J. 2007 (13) 1746.

23. U. Rohr, P. Schlichting, A. Bchm, M. Gross, K. Meerholz, C. Brauchle, K. Mullen, Angew. Chem. Int. Ed. 1998 (37) 1434.

24. M. J. Yang, S. L. Lu, Y. Li, J. Mater. Sci. Lett. 2003 (22) 813.

25. C. N. R. Rao, A. Govindaraj, in nanotubes and nanowires, RSC nanoscience and Nanotechnology series, RSC, Cambridge, UK, 2005

26. K. Sumino, I. Yonenaga, M. Imai, T. Abe, J. Appl. Phys. 1983 (54) 5016.

27. K. Sumino, M. Imai, Philos. Mag. A. 1983 (47) 753.

28. R. Sen, B. C. Satishkumar, A. Govindaraj, K. R. Harikumar, M. K. Renganathan, C. N. R. Rao, J. Mater. Chem. 1997 (7) 2335.

29. B. C. Sathishkumar, A. Govindaraj, K. R. Harikumar, J. P. Zhang, A. K. Cheetham, C. N. R. Rao, Chem. Phys. Let. 1999 (300) 473.

30. L. S. Panchakarla, A. Govindaraj, C. N. R. Rao, ACS nano. 2007 (1) 494.

31. H. M. Jeong, J. W. Lee, W. H. Shin, X. J. Choi , J. W. Choi, nano lett. 2011 (11) 2472.

32. Z. Sheng, L. Shao, J. Chen, W. Bao, F. Wang, X. Xia, ACS nano. 2011 (5) 4350.

33. Y. Wang, Y. Shao, D. W. Matson, J. Li, Y.